2002-09

Microstructure characterization of friction-stir processed nickel-aluminum bronze through orientation imaging microscopy

Cuevas, Assunta Mariela.

Monterey, California. Naval Postgraduate School

NAVAL POSTGRADUATE SCHOOL
Monterey, California

THESIS

MICROSTRUCTURE CHARACTERIZATION OF FRICTION-STIR PROCESSED NICKEL-ALUMINUM BRONZE THROUGH ORIENTATION IMAGING MICROSCOPY

by

Assunta Mariela Cuevas

September 2002

Thesis Advisor: Terry R. McNelley

THIS PAGE INTENTIONALLY LEFT BLANK

REPORT DOCUMENTATION PAGE			Form Approved OMB No. 0704-0188
Public reporting burden for this collection of information is estimated to average 1 hour per response, including the time for reviewing instruction, searching existing data sources, gathering and maintaining the data needed, and completing and reviewing the collection of information. Send comments regarding this burden estimate or any other aspect of this collection of information, including suggestions for reducing this burden, to Washington headquarters Services, Directorate for Information Operations and Reports, 1215 Jefferson Davis Highway, Suite 1204, Arlington, VA 22202-4302, and to the Office of Management and Budget, Paperwork Reduction Project (0704-0188) Washington DC 20503.			
1. AGENCY USE ONLY ***(Leave blank)***	**2. REPORT DATE** September 2002	**3. REPORT TYPE AND DATES COVERED** Master's Thesis	
4. TITLE AND SUBTITLE: Title (Mix case letters) Microstructure Characterization of Friction-Stir Processed Nickel-Aluminum Bronze Through Orientation Imaging Microscopy			**5. FUNDING NUMBERS**
6. AUTHOR(S) Cuevas, Assunta M.			
7. PERFORMING ORGANIZATION NAME(S) AND ADDRESS(ES) Naval Postgraduate School Monterey, CA 93943-5000			**8. PERFORMING ORGANIZATION REPORT NUMBER**
9. SPONSORING /MONITORING AGENCY NAME(S) AND ADDRESS(ES) Defense Advanced Research Projects Agency (DARPA), Dr. L. Christodoulou.			**10. SPONSORING/MONITORING AGENCY REPORT NUMBER**
11. SUPPLEMENTARY NOTES The views expressed in this thesis are those of the author and do not reflect the official policy or position of the Department of Defense or the U.S. Government.			
12a. DISTRIBUTION / AVAILABILITY STATEMENT Approved for public release; distribution is unlimited			**12b. DISTRIBUTION CODE**

13. ABSTRACT ***(maximum 200 words)***

The effect of friction-stir processing (FSP) on the microstructure of a cast nickel-aluminum bronze (NAB) material has been characterized by various micro-analytical methods including orientation imaging microscopy (OIM). Cast NAB is widely utilized in the production of propellers for the surface ships and submarines of the U.S. Navy due to excellent corrosion-resistance. New applications require improved mechanical properties that may be attainable using FSP to achieve localized microstructure modification. Friction between a rotating tool and the surface of the material results in a "stirring" action that, in turn, produces adiabatic heating and local softening of the material. The tool rotation results in very large shear deformations in the softened regions and thus microstructure refinement and homogenization; in effect FSP may convert an as-cast microstructure to a wrought condition in the absence of macroscopic shape change. In as-cast material, results of optical and scanning electron microscopy (using energy dispersive analysis) show an α (FCC) matrix containing globular and particulate dispersions that correspond to the κ_I, κ_{II} and κ_{IV} second phases; these represent various morphologies of the Fe_3Al intermetallic compound, which has a $D0_3$ structure. Also present are lamellar particles of κ_{III}, which is NiAl and has a B2 structure. The grain size in the α matrix is ~ 1 mm. In OIM, the microtexture and microstructure in the α (FCC) matrix may be readily obtained and analyzed. However, interatom distances in the Fe_3Al and NiAl phases differ by only about one percent and so these phases are not distinguishable from one another during OIM. Altogether, microstructure and microtexture analysis showed that there are several regions in the thermomechanically affected zone (TMAZ) of a material subjected to FSP. From base material inward toward the TMAZ, these include: annealing effects in undeformed base material; a region just inside the TMAZ in which grain deformation and C-type shear deformation textures are observed; regions of highly refined and recrystallized grains further inside the TMAZ, wherein the grain size is < 5μm; and, finally, regions of elongated, banded and twinned grain structures that suggest grain growth following recrystalliztion.

14. SUBJECT TERMS Nickel Aluminum Bronze, Friction Stir Processing, Orientation Imaging Microscopy, Electron Backscatter Diffraction, Energy Dispersive Spectroscopy, Optical Microscopy, Thermomechanically-Affected Zone, Shear Deformation.			**15. NUMBER OF PAGES** 75
			16. PRICE CODE
17. SECURITY CLASSIFICATION OF REPORT Unclassified	**18. SECURITY CLASSIFICATION OF THIS PAGE** Unclassified	**19. SECURITY CLASSIFICATION OF ABSTRACT** Unclassified	**20. LIMITATION OF ABSTRACT** UL

NSN 7540-01-280-5500 Standard Form 298 (Rev. 2-89)
Prescribed by ANSI Std. 239-18

THIS PAGE INTENTIONALLY LEFT BLANK

Approved for public release; distribution is unlimited

MICROSTRUCTURE CHARACTERIZATION OF FRICTION-STIR PROCESSED NICKEL-ALUMINUM BRONZE THROUGH ORIENTATION IMAGING MICROSCOPY

Assunta M. Cuevas
Lieutenant, United States Navy
B.S., University of California at Los Angeles, 1996

Submitted in partial fulfillment of the
requirements for the degree of

MASTER OF SCIENCE IN MECHANICAL ENGINEERING

from the

NAVAL POSTGRADUATE SCHOOL
September 2002

Author: Assunta M. Cuevas

Approved by: Terry R. McNelley
Thesis Advisor

Young W. Kwon
Chairman, Department of Mechanical Engineering

THIS PAGE INTENTIONALLY LEFT BLANK

ABSTRACT

The effect of friction-stir processing (FSP) on the microstructure of a cast nickel-aluminum bronze (NAB) material has been characterized by various micro-analytical methods including orientation imaging microscopy (OIM). Cast NAB is widely utilized in the production of propellers for the surface ships and submarines of the U.S. Navy due to excellent corrosion-resistance. New applications require improved mechanical properties that may be attainable using FSP to achieve localized microstructure modification. Friction between a rotating tool and the surface of the material results in a "stirring" action that, in turn, produces adiabatic heating and local softening of the material. The tool rotation results in very large shear deformations in the softened regions and thus microstructure refinement and homogenization; in effect FSP may convert an as-cast microstructure to a wrought condition in the absence of macroscopic shape change. In as-cast material, results of optical and scanning electron microscopy (using energy dispersive analysis) show an α (FCC) matrix containing globular and particulate dispersions that correspond to the κ_I, κ_{II} and κ_{IV} second phases; these represent various morphologies of the Fe_3Al intermetallic compound, which has a $D0_3$ structure. Also present are lamellar particles of κ_{III}, which is NiAl and has a B2 structure. The grain size in the α matrix is ~ 1 mm. In OIM, the microtexture and microstructure in the α (FCC) matrix may be readily obtained and analyzed. However, interatom distances in the Fe_3Al and NiAl phases differ by only about one percent and so these phases are not distinguishable from one another during OIM. Altogether, microstructure and microtexture analysis showed that there are several regions in the thermomechanically affected zone (TMAZ) of a material subjected to FSP. From base material inward toward the TMAZ, these include: annealing effects in undeformed base material; a region just inside the TMAZ in which grain deformation and C-type shear deformation textures are observed; regions of highly refined and recrystallized grains further inside the TMAZ, wherein the grain size is < 5μm; and, finally, regions of elongated, banded and twinned grain structures that suggest grain growth following recrystalliztion.

THIS PAGE INTENTIONALLY LEFT BLANK

TABLE OF CONTENTS

LIST OF FIGURES

THIS PAGE INTENTIONALLY LEFT BLANK

LIST OF TABLES

THIS PAGE INTENTIONALLY LEFT BLANK

LIST OF ABBREVIATIONS, ACRONYMS, AND SYMBOLS

ASTM	American Society for Testing and Materials
BCC	Body Centered Cubic
CBN	Cubic Boron Nitride
DRX	Dynamically Recrystallized
EBSP	Electron Backscatter Pattern
EDS	Energy Dispersive Spectroscopy
FCC	Face Centered Cubic
FSP	Friction Stir Processing/Processed
HAZ	Heat-Affected Zone
KV	kilovolt
NAB	Nickel Aluminum Bronze
NSWCCD	Naval Surface Warfare Center, Caderock Division
OIM	Orientation Imaging Microscopy
OM	Optical Microscopy
PSN	Particle Stimulated Nucleation
RSC	Rockwell Science Center
SC	Simple Cubic
SEM	Scanning Electron Microscope
TMAZ	Thermomechanically-Affected Zone
TWI	The Welding Institute
UNS	Unified Numbering System
Wt. %	Weight Percent
α	alpha
β	beta
κ	kappa
γ	gamma

THIS PAGE INTENTIONALLY LEFT BLANK

ACKNOWLEDGMENTS

The author would like to thank the Defense Advanced Research Projects Agency (DARPA – Dr. L. Christodoulou) for their funding and support of this ground-breaking research; Bill Palko and Steve Fielder at the Naval Surface Warfare Center (Caderock Division) for their material and technical support; and last but certainly not least, Murray W. Mahoney at the Rockwell Science Center for his support and contagious enthusiasm.

The author would like to thank Professor Terry McNelley for his invaluable guidance and support through this research project.

The author would also like to express her deepest gratitude to Doug Swisher for his tireless efforts, patience, guidance and support in teaching the ways of OIM, EDX, and meticulous sample preparation.

The author would like to thank her friends and family for their understanding, humor, patience and love during the course of this work.

Finally, the author would like to thank her fiancé for his priceless love, faith, encouragement and support, and for always helping her to remember the important things in life.

THIS PAGE INTENTIONALLY LEFT BLANK

I. INTRODUCTION

A. NICKEL-ALUMINUM BRONZE

Nickel-aluminum bronze (NAB) materials are copper-base alloys that are widely used to produce cast components for marine applications. Such applications reflect combinations of the good strength and the excellent corrosion resistance available with these alloys. NAB's are also richly endowed with many other outstanding physical properties. Some of the attributes worthy of note are [Ref. 1]: i) good fracture toughness at both extremely low and elevated temperatures, combined with moderate tensile strengths; ii) low coefficients of friction and good wearability; iii) non-sparking behavior; iv) high damping capacity; v) outstanding resistance to corrosion, which is the biggest single cause of metal deterioration in marine environments; vi) and exceptional resistance to fatigue, which is the second most common cause of metal deterioration in marine equipment. Because of these desirable properties, NAB's have been extensively used in both freshwater and seawater services, for components such as pumps, valve parts, fittings, gears, and propellers. The application of particular interest here is the U.S. Navy's use of NAB's for ship and submarine propellers.

The NAB alloy typically used for the casting of propellers is designated as UNS C95800, also known as alpha nickel aluminum bronze or propeller bronze [Ref. 2]. Nickel-aluminum bronze propellers are typically sand-cast [Ref. 3] and slow-cooled, according to ASTM B148 standard specification for aluminum-bronze sand castings [Ref. 4]. The phases and complex microstructure transformations of NAB upon gradual cooling play an important role in its material properties [Refs. 5-6]. Variations in NAB microstructure arise because of the differences in cooling rate throughout the casting. Porosity has also been observed in cast NAB, which affects the component's overall strength and corrosion resistance.

Incidences of selective phase corrosion (i.e. dealloying or dealuminification) have been observed in corrosion tests on NAB components after prolonged seawater immersion [Refs. 7-9]. It has also been observed that the welding of cast NAB, usually

in propeller fabrication and in repair of casting defects, introduces further non-equilibrium conditions and thermal stresses, which aversely affect the corrosion behavior of the alloy. Annealing heat treatments have been used to adjust the alloy's microstructure as part of the post-welding process in order to obtain more desirable properties.

Due to massively thick sections of cast NAB propellers, the extremely low cooling rates contribute to very coarse microstructures, and thus lower strengths as compared to smaller cast components or to applications involving wrought material. Nevertheless, propellers require high strength in order to withstand the large forces encountered as they cut through the water. Furthermore, damaging effects of the environment, such as corrosion and cavitation, severely decrease the service life of a propeller. Thus, it would be desirable to have methods available to selectively strengthen the surface layer of a propeller, especially if such methods do not degrade corrosion resistance. A technique to strengthen a propeller surface by locally creating a fine microstructure, while maintaining or enhancing ductility, may lead to increased cavitation resistance and higher strength. This improvement may be carried out even further as to modify the propeller design to contain less material and weight, while maintaining its high strength and cavitation and corrosion resistances.

B. FRICTION STIR PROCESSING

Friction-stir processing (FSP) is a revolutionary thermo-mechanical processing technique adapted from the concepts of friction stir welding [Ref. 10]. FSP leads to localized severe plastic deformation of a material and thus to homogenization of microstructure and grain refinement, thereby resulting in improved material properties. Little or no macroscopic shape change may occur despite the local severity of the plastic deformation. This technique involves traversing a rotating tool across the surface of a material, producing intense plastic deformation associated with a "stirring" action in the material under the tool. Typically, an FSP tool consists of a cylindrical section with a projection, or pin, at the end that is in contact with the material being processed during the tool rotation about its cylinder axis. The end of the tool surrounding the pin is

referred to as the tool shoulder. FSP is a solid-state process (i.e. the material remains solid throughout the entire process). The material is softened from the adiabatic heating caused by the high deformation rates associated with tool rotation even in the absence of slippage between the tool and material. During such intense plastic deformation material may be transferred from one side of the tool around to the other. The material is then forged by the intimate contact of the tool shoulder and the pin profile. This produces a region of intense shear deformation and, potentially, a very fine-grain size in a single pass of the tool.

Previous work has studied the effects of friction-stir processing on commercial aluminum alloys [Refs. 11-13]. These studies revealed that friction-stir processing resulted in grain refinement. Samples prepared from the thermomechanically affected zones (TMAZ) of processed material exhibited high strain rate superplasticity, as well as improved properties such as increased static strengths and increased ductility.

C. OBJECTIVES OF THIS RESEARCH

The main objectives of this research were to characterize the influence of FSP on the microstructure of an as-cast NAB material, and to analyze the evolution of its microstructure from the undeformed base metal into the TMAZ region, with emphasis on the microtexture as well as microstructure associated with the TMAZ. This was accomplished with the use of computer-aided orientation imaging microscopy (OIM) methods associated with electron backscattering diffraction (EBSD), energy dispersive spectroscopy (EDS), and optical microscopy. The OIM approach allowed for the determination of grain size in terms of regions of common lattice orientation and thereby also allowed for the determination of grain boundary disorientations in relation to location in the material. Assessment of microstructure characteristics may allow for the determination of the extent of recovery, recrystallization and grain growth in relation to FSP.

The initial phase of this work examined the limits of application of OIM to NAB materials that have been subjected to friction stir processing. This part of the work was

concerned with the capability of OIM to distinguish phases in these materials as well as to resolve features such as grain size and to determine grain-to-grain disorientations. Subsequently, OIM methods were applied to both as-cast material and to the TMAZ of a processed sample. The evolution of grain size and shape of the Cu matrix as well as the effects of deformation on the second-phase particles were of particular concern here. Also, the role of the second-phase particles in processes of grain refinement was examined. Finally, a region of the TMAZ near its boundary with the base metal was examined to assess the microtexture in regions affected mainly by deformation and recovery effects alone and in the absence of recrystallization.

II. BACKGROUND

This chapter reviews the structure and phases as well as the phase transformations of NAB materials. In order to understand the microstructures observed in large NAB cast components, e.g. propellers, this discussion will consider a typical NAB composition corresponding to Cu-9%Al-5%Ni-4%Fe (compositions in wt. pct.). This chapter will also provide background on the revolutionary technique of friction-stir processing and its remarkable effects on the mechanical properties of alloys such as commercial aluminum and magnesium alloys, as well as its application to nickel-aluminum bronze structures.

A. COPPER-ALUMINUM SYSTEM AND DEVELOPMENT OF NICKEL-ALUMINUM BRONZE

The copper-rich end of the Cu-Al binary equilibrium phase diagram is shown in Fig 2.1. Cu-Al alloys containing less than 7 wt% Al solidify as a single-phase face-centered cubic (fcc) α phase, and retain the α single-phase solid solution upon cooling to room temperature. Alloys containing greater than 9.4 wt% Al solidify as a single-phase body-centered cubic (bcc) β; however, upon slow cooling, α forms from β and any remaining β phase transforms in a eutectoid reaction at about 570°C to produce $\alpha+\gamma$.

The γ phase has been known to be deleterious to the mechanical and corrosion-resistant properties of NAB alloys. Because of its high aluminum content, the γ phase has a lower electrochemical potential than its neighboring copper-rich α phase, and thus, preferentially corrodes [Refs. 9,14]. This preferential corrosion of aluminum is commonly referred to as dealuminization, similar to the dezincification of brass. Therefore, steps are taken to retard the formation and growth of the undesirable γ phase without otherwise compromising the alloy's mechanical properties. Generally, alloys containing γ are less strong and ductile than NAB alloys [Refs. 9,14]. It has been found that the addition of other alloying elements has proven to be the most successful method of retarding the γ phase formation.

Addition of nickel and iron to the Cu-Al alloy was found to extend the α phase field and allow for greater additions of Al without encountering the formation of the γ phase [Refs. 9,15], as seen in Figure 2.2. The Ni and Fe alloying additions result in the precipitation of complex intermetallic κ phases from the α and β phases and have been found to considerably increase NAB's mechanical properties.

Increases in the aluminum content of NAB alloys to values within the range of 8.8 - 10 wt. % have been linked to increased strength, hardness and corrosion resistance [Ref. 15]. However, this is also accompanied by a decrease in elongation, which has been attributed mainly to the presence of the lamellar κ_{III} phase along the grain boundaries [Ref. 15]. Alloys with a content of 9.5 wt% Al have been reported to give the best overall property combinations for the manufacture of propellers, combined with the following additional intentional alloying additions: 5 wt. % nickel, 4 wt. % iron, and 0.5 wt. % manganese.

Alloys containing more than 3 wt. % Fe have been reported to exhibit reduced grain size and restricted elevated temperature grain growth [Ref. 15]. Also, the solidification range is reduced. Compositions including 3 - 5 wt. % Fe [Ref. 15] have also been observed to exhibit increased strength, and strength retention at high temperatures. Such compositions also show improved wear and abrasion resistance and increased fatigue endurance limits [Ref. 15]. The optimum value of 4 wt. % Fe has been shown to give the best combination of properties [Ref. 15].

The addition of 0 - 5 wt. % Ni has been noted to increase strength, as well as to have the same grain refining effect as Fe [Ref. 15]. The addition of Ni has also been reported to retard the transformation of β phase during cooling and increase hardness [Ref. 15]. However, an alloy with a nickel concentration less than that of the iron concentration may become susceptible to severe second-phase attack in seawater, with an associated decrease in strength [Ref. 15]. For maximum corrosion resistance, it has been found that the nickel content should be greater than that of the iron, ideally 5 wt. % Ni and 4 wt. % Fe [Ref. 15].

B. NICKEL-ALUMINUM BRONZE

Nickel-aluminum bronze is a copper-base quaternary alloy with a chemical composition as listed in Table 2.1. Numerous investigators have characterized the chemistries, microstructures and crystallographic characteristics of the as-cast NAB alloy [Refs. 8-9,14,16-24]. As seen in Figure 2.2, at a nominal 9 wt. % Al content, NAB solidifies to form a single-phase β body-centered cubic (bcc) solid solution. Upon further cooling, the β-phase decomposes by formation of the face-centered cubic (fcc) α-phase and subsequently, by further transformation to α containing various κ phases. This sequence is summarized in Figure 2.3, which is from Culpan and Rose [Ref. 14]. Weill-Couly and Arnaud [Ref. 24] have classified the κ phases into four distinct types, κ_I, κ_{II}, κ_{III} and κ_{IV}, on the basis of the various morphologies observed through the optical microscope. The classification is also based in part on the sequence of formation of these phases during cooling. Figure 2.4 illustrates the typical phase distribution in the microstructure of a cooled NAB alloy. One point to note is that, due to non-uniform cooling of propeller castings, rapidly cooled, or quenched β-phase regions may also persist, and these transform into a martensitic product.

	Cu	Al	Ni	Fe	Mn	Si	Pb
min-max	min 79.0	8.5-9.5	4.0-5.0	3.5-4.5	0.8-1.5	max 0.10	max 0.03
nominal	81	9	5	4	1	-	-

Table 2.1: Chemical composition percent by weight of typical nickel-aluminum bronze. (Ref. 2)

1. Alpha (α) Phase

The light-gray areas in Figure 2.3(a) are the copper-rich α phase. The α phase is the equilibrium terminal solid solution, having a face-centered cubic (fcc) crystal structure, with a lattice parameter, a = 3.64 Å [Ref. 19]. The α phase may exhibit a Widmanstätten morphology. During cooling, proeutectoid α forms from the β phase beginning at about 950°C. At about 580°C a eutectoid reaction results in a mixture of α and κ_{III} phases. Also, κ_{IV} particles precipitate from within the α matrix during cooling.

Jahanafrooz et al. [Ref. 21] observed that, upon slow cooling from the β phase, a Widmanstätten proeutectoid α phase precipitated both intergranularly and intragranularly. The intragranular precipitation was observed to be more prevalent in coarse-grained alloys, such as large castings, i.e. propellers, which may exhibit very slow cooling rates.

2. Kappa (κ) Phases

Upon cooling, the Ni-Fe-Al κ-phases precipitate from the α and β phases. According to Weill-Couly and Arnaud [Ref. 24], the κ-phases are classified into four distinct types, κ_I, κ_{II}, κ_{III} and κ_{IV}, according to their observed distinct morphologies. Again, the phase decomposition sequence upon cooling of an NAB alloy is summarized in Figure 2.3.

a. Kappa I (κ_I) Phase:

The κ_I phase is the large, dendritic (rosette-shaped) particle that has been observed only in NAB's with iron content of greater than 5 wt. % Fe [Refs. 19,21]. The iron-rich κ_I particles, typically 20 to 50 μm in size, are located in the centers of α grains. Jahanafrooz et al. determined that the κ_I phase has a $D0_3$ lattice structure, with chemical composition close to Fe_3Al. The $D0_3$ structure is considered to be an ordered bcc superlattice, defined by eight cells, as shown in Figure 2.5 (a).

It has been proposed that in NAB alloys of high iron content, κ_I particles form from the β phase during the early stages of cooling, growing large and acting as nucleation sites for the α phase [Ref. 21]. This suggests that the β + κ region in Figure 2.2 extends upward and to the left in such alloys. Therefore, in as-cast microstructure, the large κ_I particles seem to be always surrounded by the α phase.

b. Kappa II (κ_{II}) Phase:

Similar to the κ_I composition and structure, κ_{II} is an iron-rich dendritic particle (also described as globular or rosette-shaped), although somewhat smaller than a κ_I particle, 5 to 10 μm in diameter. However, large κ_{II} particles may easily be mistaken for κ_I. The κ_{II} precipitates have also been shown to have a $D0_3$ structure, with a lattice

parameter, a = 5.71 Å [Ref. 19]. Note, in Figure 2.5, that the κ_{II} phase is an "ordered version" of the disordered, high temperature β phase, thus explaining its dendritic morphology. κ_{II} particles have been observed to occur in the lamellar eutectoid region of the microstructure and form within the same temperature range as the Widmanstätten α phase.

c. Kappa III (κ_{III}) Phase:

At about 580°C, a nickel-rich lamellar (or globular) eutectoid form of the κ-phase, κ_{III}, precipitates from the β phase. It has been observed that initial precipitates of κ_{III} are globular with subsequent precipitates being lamellar. Previous research [Ref. 19] has shown that the κ_{III} phase has the NiAl composition and a corresponding B2 structure, with a lattice parameter, a = 2.88 Å [Ref. 19]. This is lattice parameter is approximately half the lattice parameter of the κ_{I}, κ_{II}, and κ_{IV} phases. As shown in Figure 2.5 (b), the B2 structure for NiAl is an ordered structure (also more commonly known as the CsCl type structure), which can be compared with the κ_{II} phase in its similarity to the "ordered version" of the β phase [Ref. 19,25]. Therefore, it is likely that the κ_{II} particles may act as a substrate for the formation of κ_{III} particles [Ref. 25].

It has been proposed [Ref. 25] that proeutectoid α is the "active nucleus" for the initiation of the β eutectoid decomposition into $\alpha + \kappa_{III}$. In other words, the precipitation of κ_{III} on the proeutectoid α/β interface is the only nucleation event required for the development of a eutectoidal colony. The re-nucleation of α is not necessary to form the eutectoidal colonies [Ref. 25].

d. Kappa IV (κ_{IV}) Phase:

The fine cruciform equiaxed particles distributed throughout the α grains are the iron-rich κ_{IV} particles. These precipitates are small, on the order of less than 2 μm in diameter [Ref. 19]. Having the same Fe_3Al composition as κ_{I} and κ_{II} phases, κ_{IV} particles also have a $D0_3$ crystal structure, and have a lattice parameter, a = 5.77 Å [Ref. 19]. As can be seen in Figure 2.4 (a) and (b), a precipitate free zone (PFZ) is present at the periphery of the α grains.

e. Martensitic Beta (β'):

It was found that as the transformation temperature decreased, the decomposition rate of β also decreased at lower temperatures [Ref. 15,25]. Therefore, it is possible for the β decomposition to be incomplete at normal cooling rates. As the reaction slows and ceases, any remaining β undergoes a diffusionless shear transformation to martensite β'.

Several factors affect the mechanical properties of cast NAB structures. Due to the slow cooling rates in large cast NAB components, strengths and microstructures vary within the casting. Processing of cast structures may also lead to inconsistent chemical compositions, containing more or less of the nominal alloying element compositions necessary for corrosion resistance and strength. In addition to these issues, porosity introduced in the casting process further lowers the material's strength and cavitation resistance.

During its service life, a propeller may experience many stresses and phenomenons that challenge its mechanical properties and resistances. One such phenomenon, cavitation, is a widely recognized enemy of propeller material. Cavitation occurs when a propeller turns at high speed, and the resulting high relative velocity of the propeller surface and the water, augmented by surface irregularities, results in a tendency to form a vacuum adjacent to the propeller. When the absolute pressure is reduced below the vapor pressure of the fluid, vapor pockets are formed, which break the continuity of flow and reduce the efficiency of the propeller. When the cavitation bubbles collapse on the blade surfaces due to condensation, erosion of these surfaces may result. Cavitation thus degrades the propeller material. Porosity in a cast propeller intensifies the erosion caused by cavitation.

These pertinent concerns have been incorporated into the maintenance and service life of NAB components, i.e. propellers. With the high cost of manufacturing and maintaining such massive components, improvements to the alloy's strength and mechanical properties may significantly contribute to lengthening its service life and time

between overhauls, reduce maintenance cost, and open the door to enhanced design modifications.

C. FRICTION STIR PROCESSING

Friction stir processing (FSP) is an innovative new technique that locally alters the microstructure of a material's surface, producing a fine microstructure and improved material properties. FSP has been adapted from friction stir welding (FSW), which was invented and developed at The Welding Institute in 1991 [Ref. 10]. In friction stir processing, the surface of one material is processed, instead of joining two materials together, as done in friction stir welding. The surface of the FSP material is stirred as in FSW, resulting in a fine microstructure.

In friction stir processing, a wear-resistant cylindrical tool consisting of a small diameter pin with a concentric larger diameter shoulder is rotated and plunged into the selected metal surface, as illustrated in the schematic of Figure 2.6. The metal sample is clamped down to prevent movement during the process. The tool is then traversed along the surface of the material for single- or multi-pass processes. Friction and deformation between the rotating pin and the surface rapidly heats and softens a small column of metal but does not melt it. (Note that little of the heating does originates from slippage, i.e. there is little or no slippage between the tool and the material surface. Most of the heating is due to deformation of the metal under adiabatic conditions) The softened metal is then stirred by the rotation of the tool. Contact between the rotating shoulder and the metal surface creates additional frictional heat and plasticizes a larger cylindrical metal column around the inserted pin. Depth of penetration is controlled by the tool shoulder and length of the pin. The shoulder also acts to contain the upward metal flow caused by the insertion and rotation of the tool pin. The tool and the area to be processed are moved relative to each other; overlapping of passes during multi-pass FSP may be employed to assure complete refinement of the processed surface of the material. Hot working by the rotating tool plasticizes the metal within a narrow zone and transports it from the advancing side to the retreating side of the tool. This stirring action produces a highly deformed area with a fine microstructure. The deformed region may be devoid of

porosity. A defect-free, fine-grained recrystallized microstructure forms as the processed zone cools.

This recrystallized zone produced from FSP has also been observed during friction-stir welding of high strength aluminum alloys [Refs. 26-27]. In a study by Jata and Semiatin [Ref. 26], the weld nugget produced by FSW of an aluminum alloy appeared to be comprised of equiaxed, fine, dynamically recrystallized grains, whose size was found to be substantially smaller than the grain size in the parent material. Additionally, a severe distortion of the grain structure was observed in the FSW thermomechanically-affected zone (TMAZ). The study also showed noted that original grain and subgrain boundaries appeared to be replaced with fine, equiaxed recrystallized grains in the FSW nugget. The grains observed in the weld nugget were determined to be high-misorientation subgrains relative to the subgrains in the base metal, and this was cited as evidence of a continuous dynamic recrystallization process. In a study by Liu et al. [Ref. 27], it was proposed that the FSW development is dominated by slip deformation and that recrystallization evolves by dynamic continuous recrystallization, where subgrains form and induce a continuous increase in misorientation. Since FSP and FSW have such similar processes, both involving intense shear deformation by a rotating tool, it is to be anticipated that they might have comparable results.

A study by Field et al. [Ref. 28] involving the FSW of aluminum alloys indicated the presence of severe and identifiable texture gradients through the weld nugget and surrounding regions of an FSW weld. A dominant shear direction aligning with the tangent to the rotating tool was also observed.

Microstructures resulting from FSP do not have a uniform grain size distribution for any one set of processing parameters. Grain size varies from the top to the bottom as well as from the advancing to the retreating side of the tool. The differences in grain size likely are associated with differences in both peak temperature and times at temperature.

The processed material experiences high strain, strain rate and temperature gradients as well as grain size gradients in a very short distance. Although comparable to the heat-affected zone (HAZ) encountered in conventional fusion weldments, the thermo-

mechanically affected zone, or TMAZ, in a friction-stir processed metal does not exhibit the low strength or undesirable properties typically caused by the high temperatures during the welding process. In fusion welding, melting temperatures are reached and exceeded, allowing for grain growth and alloy segregation in the HAZ, consequently lowering its strength and corrosion resistance. On the contrary, since FSP is a solid-state process, temperatures do not reach melting temperatures, reducing the extent of grain growth in the affected area. The resulting TMAZ in a friction-stir processed metal has a finer microstructure than the base metal, increasing its strength as well as improving its properties.

In addition to the ability to locally refine the surface microstructure of a material leading to higher strengths, friction stir processing also has other advantages. As mentioned earlier, the FSP zone is devoid of porosity. Since it is a solid-state process (i.e. no melting of the material occurs during the process), the detrimental grain growth, decreased strength and increased corrosion susceptibility normally associated with weld HAZ regions are avoided. As previously noted, alloys which have been difficult or nearly impossible to weld, e.g. 7000 series aluminum alloys, have been easily processed, resulting in improved properties. Also, no gas shielding is required for oxide-forming metals. The non-consumable tool may be used for many processes, and is thus cost-efficient. Little to no noise is emitted during the process. The process may be performed in nearly all environments since no fumes or gases are released. No special cleaning techniques or material preparations are required prior to processing.

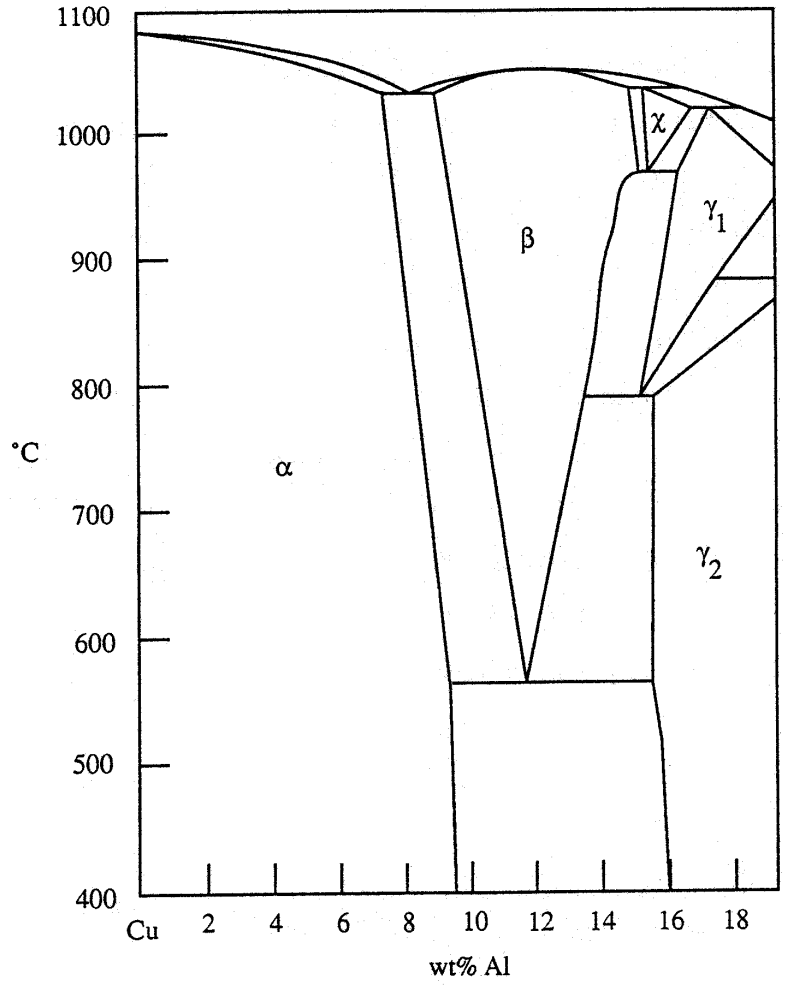

Figure 2.1: Copper-rich end of the Cu-Al phase diagram. (Ref. 2)

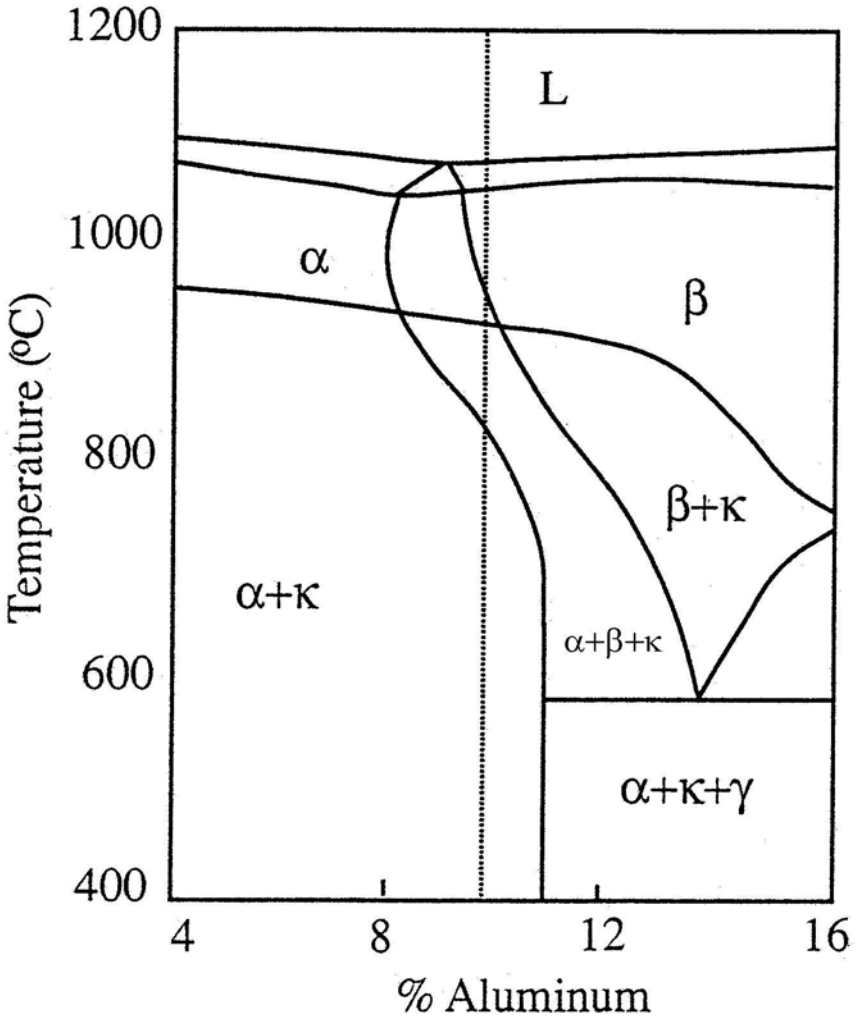

Figure 2.2: Vertical section through Cu-9%Al-5%Ni-5%Fe phase diagram. (Modified from Ref. 16)

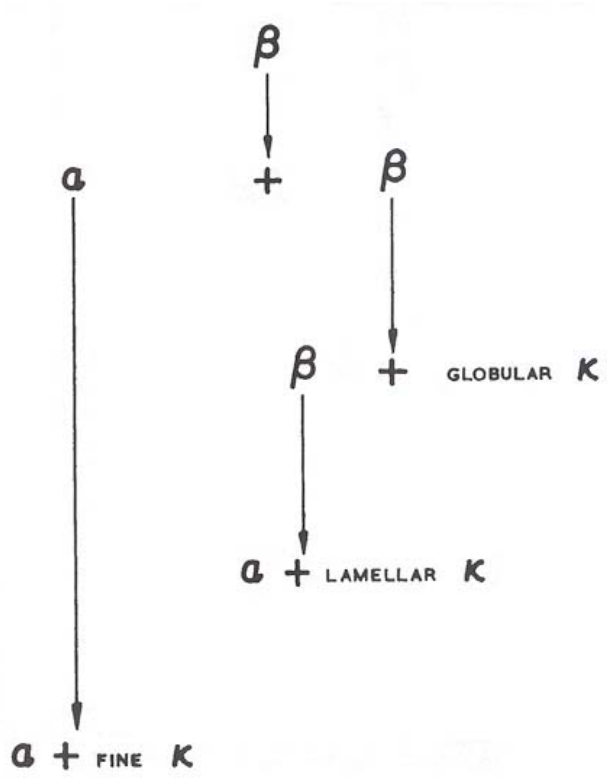

Figure 2.3: Schematic representation of β phase breakdown of NAB alloy (Ref. 14).

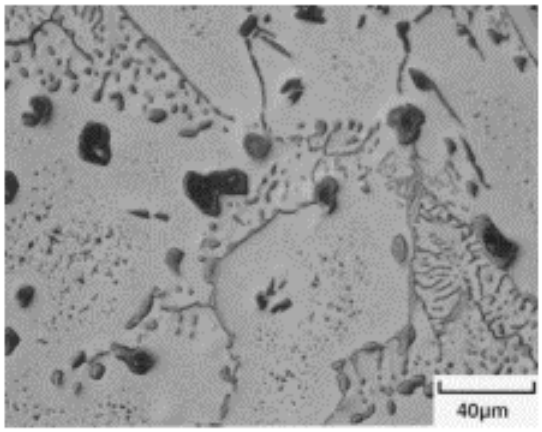

(a)

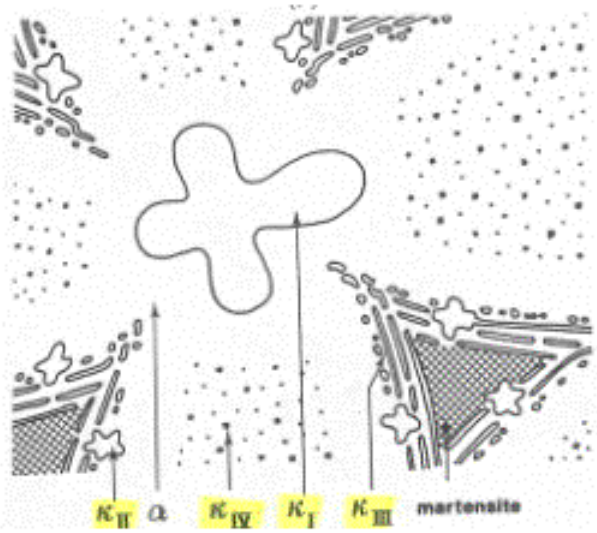

(b)

Figure 2.4: (a) Optical micrograph of cast NAB *(Courtesy of M.W. Mahoney, RSC)*. (b) Schematic microstructure distribution in cast NAB [Ref 19]. Upon continuous cooling, the β phase transforms into α-matrix and κ phases. κ_I is large, globular and dendritic, with sizes on the order of 20 to 50 μm in diameter. κ_{II} is smaller, globular and dendritic, approximately 5 to 10 μm in diameter. κ_{III} takes on a lamellar, eutectoid form. κ_{IV} is the fine cruciform phase that precipitates within the α-matrix, with a diameter less than 2 μm.

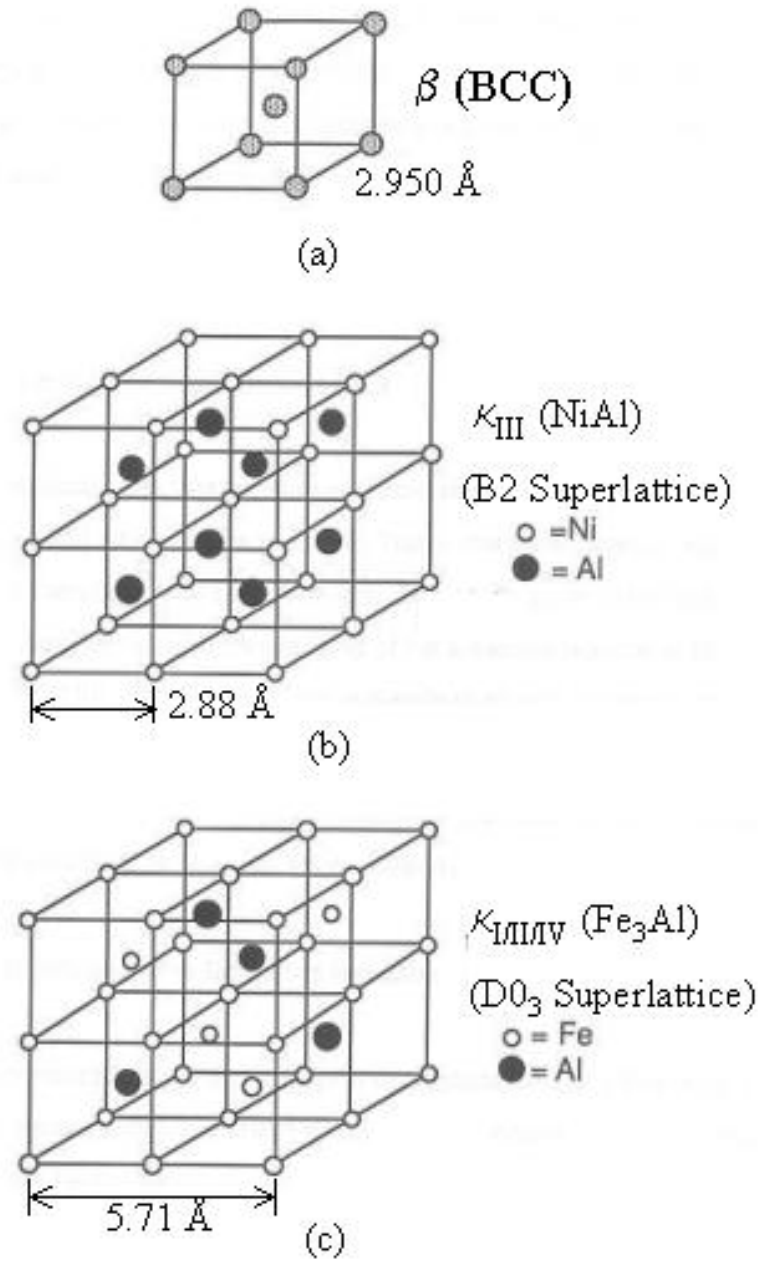

Figure 2.5: Lattice structures of NAB phases. (a) BCC β, (b) κ_{III}-phase B2 (NiAl), and (c) $\kappa_{I/II/IV}$-phase $D0_3$ (Fe_3Al) structures. (Modified from Ref. 19)

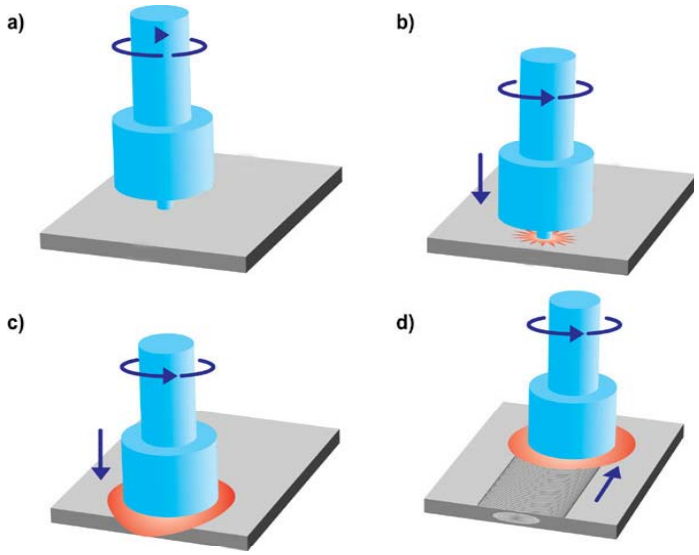

Figure 2.6: Friction stir process. a) A non-consumable cylindrical FSP tool is rotated at high speeds and plunged into the metal surface (b). Initial pin entry creates frictional heating. (c) Contact between the metal surface and tool shoulder creates a column of softened, plasticized metal and additional heat by shear deformation. The softened material is then "stirred" by the rotating motion of the tool. (d) The tool traverses the metal surface, leaving behind a fine recrystallized microstructure. *(Courtesy of M.W. Mahoney, RSC)*

THIS PAGE INTENTIONALLY LEFT BLANK

III. EXPERIMENTAL PROCEDURES

A. SAMPLE PREPARATIONS

An as-cast nickel-aluminum bronze (NAB) plate, approximately 250 mm square and 40 mm in thickness, was provide by the Naval Surface Warfare Center, Carderock Division (NSWC-CD). The chemical analysis data in Table 3.1 were obtained from Anamet Laboratories, Hayward, CA. The nickel content of this particular material falls below the accepted composition limit for this element (Table 2.1). Samples of this as-cast NAB material were sectioned using a Buehler saw with a diamond-wafering blade. Annealing treatments were conducted with a NEY 2-160 Series II furnace (± 2°C).

Mechanical polishing of the as-cast samples was accomplished following the steps outlined in Table 3.2 for the indicated times. The silicon carbide (SiC) paper was used with water as the lubricant on a flat surface, polishing in one direction until all evidence of prior polishing was eliminated. The sample was then rotated 90° and the process was repeated.

After each mechanical polishing step, an ultrasonic cleaning was performed for 10 minutes in ethanol.

A high quality finish was required due to the very small interaction volume of the electrons near the surface of the sample. Hence, the final polishing step was an electropolish at 30 volts for 10 seconds in a Buehler Electromet 4 using a 33% Nitric Acid-66% Ethanol electrolyte solution that was cooled to -25°C without etching.

A friction-stir processed nickel-aluminum bronze (FSP NAB) sample (Figure 3.1), designated FSP 379, was received from the Structural Materials Department of Rockwell Science Center (RSC) in Thousand Oaks, California. Although details of the tool geometry were not available, the processing conditions were as listed in Table 3.2. The sample was sectioned and mounted in such a way that the direction of tool travel was into the plane of the sample. The tool rotation was carried out such that the advancing side (i.e. the side which travels in the same direction as the tool advance) was on the right

side, while the retreating side (i.e. the side which travels opposite to the direction of tool advance) was on the left side, as shown in Figure 3.1.

Sample preparation for this FSP NAB sample were conducted at RSC using similar procedures as previously stated, excluding the 1-μm diamond suspension polishing step. Etching of the FSP NAB sample for optical microscopy was prepared at room temperature using a two-step process:

1. Ammonium hydroxide solution: 40 % ammonia – 20 % hydrogen peroxide – 40 % water (1-2 seconds)
2. Phosphoric hydroxide solution: 40 % phosphoric acid – 10 % hydrogen peroxide – 60 % water (1 second)

Electrolytic etching for the FSP NAB was conducted at RSC using a 75 % methanol – 25 % nitric acid cold solution, at 15 volts.

B. OPTICAL MICROSCOPY

Optical microscopy of the as-cast and FSP NAB samples was conducted with a JENAPHOT 2000 Reflected-Light photomicroscope, equipped with a SEMICAPS Genie SEM digital imaging system.

C. ENERGY DISPERSIVE X-RAY ANALYSIS

A TOPCON SM-510 Scanning Electron Microscope (SEM) with a tungsten filament was used, supplemented with an energy-dispersive x-ray detector from EDAX, Inc. and an ISIS software program. The ISIS program allowed for collection and analysis of energy spectrum for each sample scan in order to identify the major components in the alloy. Using the energy signatures of the major components, an area of the sample was then scanned to reveal concentrations of the alloy components. This helped identify locations of high nickel and iron content, which concurred with the compositions of the NAB complex phases. A 99.999% pure Cu was used for quant calibration prior to each analysis.

Cu	Al	Ni	Fe	Mn	Zn	Si	Sn	P	Pb
81.2	9.39	2.04	3.67	1.20	0.14	0.05	0.02	0.009	<0.005

Table 3.1: Composition of as-cast nickel-aluminum bronze received from NSWCCD.

Tool rotation speed	800 rpm
Tool travel speed	1 inch per minute
Tool tilt	3 degrees
Tool shoulder diameter	0.934 inches

Table 3.2: Friction-stir processing conditions for Rockwell FSP 379. (Courtesy of M.W. Mahoney, RSC)

Step	Abrasive	Time	RPM
1	500 Grit SiC Paper	30 sec.	n/a
2	1000 Grit SiC Paper	30 sec.	n/a
3	2400 Grit Sic Paper	30 sec.	n/a
4	4000 Grit SiC Paper	30 sec.	n/a
5	3 μm Metadi Diamond Suspension	10 min.	180
6	1 μm Metadi Diamond Suspension	10 min.	180
7	0.05 μm Colloidal Silica	15 min.	50

Table 3.3: Mechanical Polishing

D. ORIENTATION IMAGING MICROSCOPY (OIM)/ELECTRON BACKSCATTER PATTERN (EBSP) COLLECTION AND ANALYSIS

A TOPCON SM-510 Scanning Electron Microscope (SEM) with a tungsten filament was used with an accelerating voltage of 20KV. After polishing, the samples were put into the SEM in a holder that inclines the sample 70° to the horizontal. This was done in order to utilize the EBSP analysis capability of the Orientation Imaging Microscopy (OIM) hardware and software from TEXSEM Inc., shown schematically in Figure 3.2(a). Figure 3.2(b) and (c) represent the orientation of the NAB sample as viewed from the camera position.

External reference axes are necessary for OIM; these were defined as follows: the reference direction (RD) was assigned as positive downward; the normal direction (ND) was directed toward the phosphor screen, and transverse direction (TD) was parallel to the horizontal. In the case of the FSP NAB sample, ND also represents the direct opposite of the processing direction (i.e. processing direction was into the sample). Lattice orientations may then be defined in terms of Euler rotation angles that bring the cube axes of the lattice into coincidence with the reference axes.

The electron beam from the SEM was operated in spot mode with a beam diameter less than 0.2 μm. The electrons interacted with the first 30-50 nm of the sample surface, undergoing Bragg diffraction. The diffracted electrons then impinged upon a phosphor screen, thus illuminating it. A low light level camera captured the images from the phosphor screen and the OIM equipment analyzed the pattern. Figure 3.3 shows a representative Kikuchi pattern before and after indexing, with the corresponding pole figure and lattice orientation.

The OIM software allows the collected pattern to be analyzed, indexed and ranked against other possible indexing solutions. The pattern is assigned a best-fit indication called the Confidence Index (CI). If the CI is greater than 0.1, the pattern has a 95% probability of being indexed correctly. For each pattern the following data are then saved: the x – y coordinates on the sample for the point; the phase corresponding to the point; the Euler angles describing the lattice orientation at the point; the Confidence

Index; and an Image Quality (IQ) parameter that describes the sharpness of the observed Kikuchi pattern.

Various combinations of these parameters may then be used to create visual representations of spatial distribution of, for example, crystallographic orientation, or image quality (IQ) of the diffraction images. Orientation data may be presented as grain orientation maps, pole figures, histograms of the grain-to-grain misorientation angles, etc. Here, misorientation angle refers to the minimum rotation angle among all crystallographically equivalent rotations that bring neighboring lattice orientations within the same phase into coincidence. Various data clean-up steps are performed and typically involve three successive steps. First, individual points that do not belong to any grains are assigned to match the neighboring majority grain. Second, the highest CI for a grain is assigned to all points in that grain. Third, data points with CI's less than 0.1 are compared to those of nearest neighbors and the neighbor with the highest CI is reassigned to that point, thus effectively making it a point in that grain. This clean-up step assumes that the low CI points are located near grain boundaries or areas of high dislocation density and that the point with the higher CI is the true orientation for the low CI point. It should be noted that any single point with a CI greater than 0.1 will not be altered by this procedure. Grains with good quality EBSP's, no matter what size, will be saved unchanged. The elimination of low CI points was done in order to obtain a true picture of the grain boundaries and the angular disorientation between grains. After the clean up procedure is completed, the OIM software is used to produce OIM grain maps, pole figures and rotation angle histograms, as described previously. Further discussion of phase identification will be provided subsequently when the results of analysis of the as-cast and FSP NAB samples are presented. While it is possible to conduct OIM on multi-phase materials this area of the technique is less well developed than orientation determination and analysis.

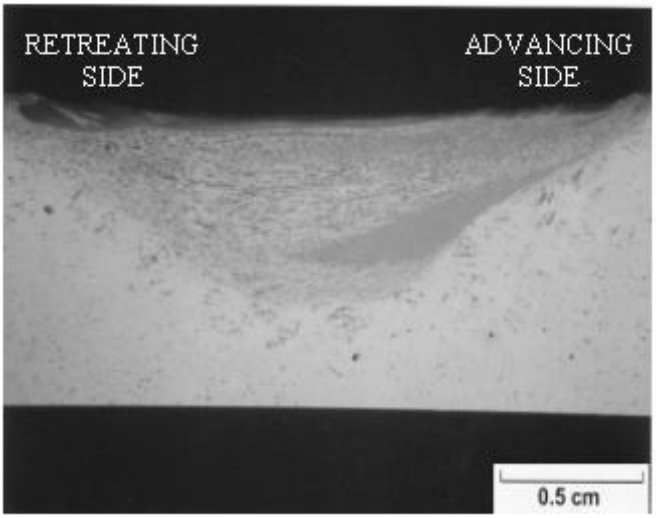

Figure 3.1: Optical micrograph of FSP 379 friction-stir processed nickel-aluminum bronze provided by Rockwell Science Center, Thousand Oaks, California.

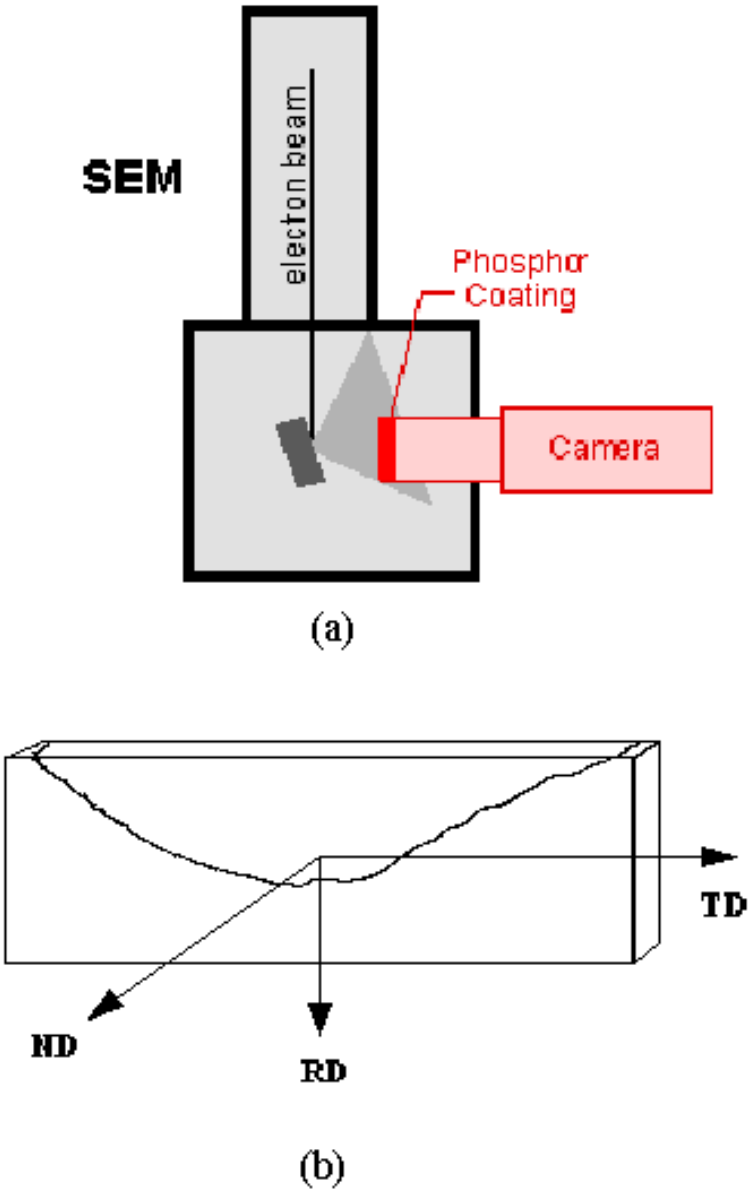

Figure 3.2. (a) A simplified schematic of the Orientation Imaging Microscopy set-up in the SEM, and the sample directions (b) in the microscope.

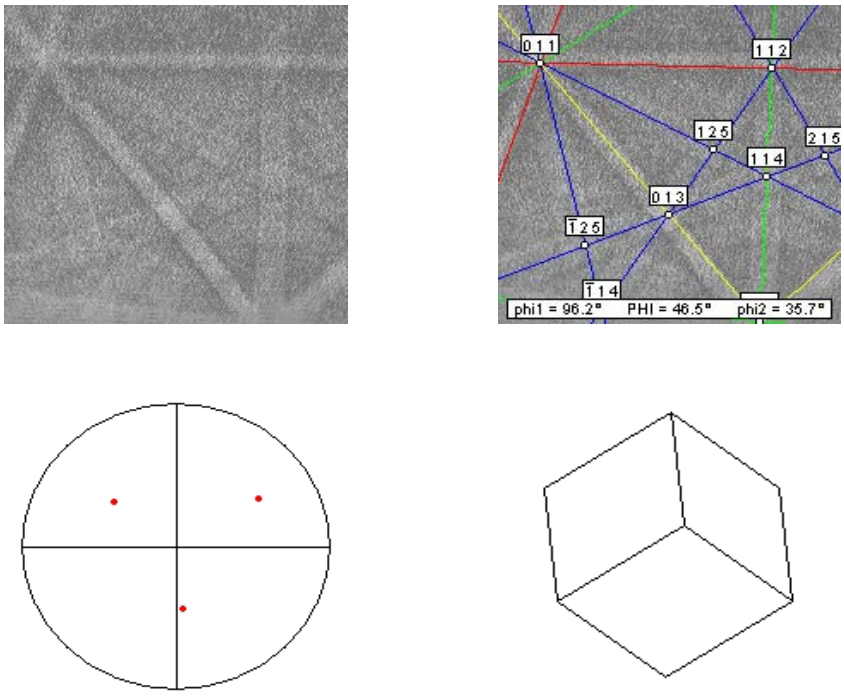

Figure 3.3. Sample Kikuchi pattern and indexing. In (a), an actual Kikuchi pattern obtained on the video screen is shown; (b), an indexed pattern showing several low-index poles [011], [112], [125], etc.; and Euler angles phi1, PHI and phi2 for this orientation. A pole figure is shown in (c), representing the orientation of the indexed pattern for the <100> poles. Cubic crystal (d) orientation represented by this pattern.

IV. RESULTS AND DISCUSSION

This chapter discusses the application of Orientation Imaging Microscopy (OIM) to the analysis of NAB and friction-stir processed NAB, as well as the results of other conventional analysis techniques (i.e. optical microscopy and energy-dispersive x-ray analysis) that were applied to the NAB. Of particular concern are the limitations of OIM as well as its capabilities as applied to NAB microstructures.

A. ORIENTATION IMAGING MICROSCOPY (OIM) REVIEW

Orientation imaging microscopy (OIM) is a useful tool for the analysis of local texture and certain grain boundary characteristics in polycrystalline materials. The OIM software of interest here (TSL/EDAX, Inc.) consists of both a data collection program and a data analysis program. The OIM Data Collection software [Ref. 29] enables thousands of orientation measurements and phase analyses to be rapidly recorded for a specific area scan. OIM Analysis [Ref. 30] and its features may then be used to analyze the orientation data and phase distributions.

The capabilities of OIM have become widely appreciated in the analysis of pure and simple alloys that contain one or, at most, two phases having crystal structures that are readily distinguishable [Refs. 28, 31-32]. Diffraction patterns of distinct phases with different crystal structures have been observed to be easily identifiable and distinguishable, and thus contributed to the ease in analysis of grain orientation. However, analysis of multi-phase alloys, especially when two phases are expected to exhibit nearly identical diffraction patterns, has not been reported in the literature.

In order to understand the results obtained here it is useful to provide further details of OIM analysis. Parameters of a sample are initially entered in the OIM data collection system. These include anticipated crystal structure(s) and lattice parameter(s), as well as phase nomenclature. From a sample tilted at 70 degrees in the SEM, the OIM data collection software rapidly captures electron backscatter diffraction pattern (EBSP) images from a phosphor screen using a low-light camera. At each point in a raster-like pattern on the sample surface the data that are obtained and recorded are: x - y

coordinates of the point; the phase identification; the lattice orientation (defined by three Euler angles); the image quality (IQ), and the confidence index (CI).

When attempting to identify the phase at a point during a scan, the OIM data collection system compares the detected EBSPs with diffraction patterns that are calculated based on an initial input of crystal structure types and lattice parameters into the software. The detected patterns are compared to the input pattern(s) in the order that the inputs are listed. The default is to the first one on the list in the absence of a satisfactory match to any of the other entries. The data point is then assigned to the phase most closely matching the detected diffraction pattern. A corresponding confidence index is assigned to the data point which takes into consideration the ability of the software to accurately match phases and crystal orientations.

B. AS-CAST NICKEL-ALUMINUM BRONZE

As-cast NAB samples, with a chemical composition as listed in Table 3.1, were analyzed using optical microscopy and energy-dispersive x-ray analysis, as well as using the OIM program.

1. Optical Microscopy

Optical microscopy of the as-cast NAB microstructure resulted in findings similar to those described in literature [Refs. 8-9,14,16-24]. A typical microstructure is shown in Figure 4.1. The α and κ phases are labeled according to their morphologies. The globular, dendritic κ_{II} particles were apparent, with the finer and dendritic κ_{IV} particles present within grain interiors of the α matrix. The eutectoidal lamellar κ_{III} phase was observed as well. Due to the low nickel and iron contents, the κ_I phase was not observed.

2. Energy-Dispersive X-ray (EDX) Analysis

EDX analysis was also conducted to further distinguish between second phase particles and verify chemical compositions. In Figure 4.2(b), the matrix stands out in the Cu K_α X-ray map, which concurs with its identification as the fcc α phase. As can be seen in Figure 4.2(c), the globular particles may be distinguished in the Fe K_α X-ray map, which is consistent with the iron-rich (Fe_3Al) composition of the κ_{II} particles. Likewise,

in Figure 4.2 (d), the lamellar particles are more apparent in the Ni K_α X-ray map, which supports their morphological identification as the nickel-rich (NiAl) κ_{III} particles.

3. OIM

Crystal orientations and phase identifications were obtained for an as-cast NAB sample using OIM. The lattice parameters for the α and κ phases, as given in Chapter II, were entered into the OIM data collection program, designating the α phase as an fcc structure, with a lattice parameter, a_α = 3.64 Å, and both κ particle types ($\kappa_{I,II,IV}$ and κ_{III}) as ordered cubic crystal structures, with lattice parameters $a_{\kappa I,II,IV}$ = 5.71 Å and $a_{\kappa III}$ = 2.88 Å, respectively. The B2 and $D0_3$ superlattice structures are have not been included in the OIM software and so initially bcc was used. Recall from Chapter II that the lattice parameter of the nickel-rich κ_{III} particle (B2 crystal superlattice) is almost exactly one-half that of the iron-rich $\kappa_{I,II,IV}$ particle ($D0_3$ crystal structure). Thus, with almost identical interatomic distances, these two κ phase types would only be distinguishable by the differences in their diffraction intensities.

a. Phase Identification Limitations:

A scanned area of the as-cast NAB microstructure is represented by the green box in Figure 4.3 (a). From its size and morphology alone in Figure 4.3 (a), the globular dendritic particle was identified as the κ_{II} phase, surrounded by the α matrix. The OIM software clearly identified the fcc α matrix in Figure 4.3 (b), designated it using an arbitrarily chosen solid maroon color, and distinguished it from the ordered κ_{II} phase. However, in Figure 4.3 (c), it becomes apparent that the OIM software was unable to distinguish between the nearly identical diffraction patterns obtained from the $\kappa_{I,II,IV}$ and κ_{III} phases. Additionally, the software was unable to detect the differences in diffraction intensities from the two separate κ phase types. Thus, the OIM software defaulted to what appears to be a systematic interpretation of the orientation data, switching between $\kappa_{I,II,IV}$ and κ_{III} phases which resulted in the rainbow pattern in Figure 4.3 (c).

Attempts were made to adjust the parameters initially entered into the OIM program to more accurately represent the phases at hand. Keeping the associated lattice parameters for the fcc α matrix and κ phase types unchanged, the crystal structures

of the κ phase types were both modified to reflect simple cubic structures rather than bcc. The results were the same systematic default interpretation (i.e. rainbow-like pattern) as shown in Figure 4.3. Finally, the attempt to identify α and a single κ phase, with a lattice parameter of a_κ = 2.88 Å proved successful, as shown in Figure 4.4. Thus, OIM has the ability to distinguish between α and κ phases, but not among κ phases. In order to discriminate between $\kappa_{I,II,IV}$ and κ_{III} phases it will be necessary to modify the OIM software to facilitate analysis of intensities as well as positions of Kikuchi lines, or perhaps to supplement OIM results with EDX data to assist in phase identification.

b. Limit of Spatial Resolution:

The ability to resolve second-phase particles in OIM grain maps was limited by the particle size. Particles, with one dimension of about 2 μm or less, were detected in secondary SEM images as well as the OIM image quality maps; this circumstance reflects that the image quality will be degraded when diffraction patterns from particles and matrix are present simultaneously. However, particles below this size were not apparent in the grain orientation maps; this may be seen by comparison of the microstructure data in Figures 4.5 (b) through (d). This circumstance reflects the overlap of diffraction patterns from the α matrix with those from the κ particle, such that a relatively stronger fcc α phase diffraction pattern is more readily indexed than a weaker pattern associated with the κ particle. Thus, the finer particles became included with the α matrix, as shown in Figures 4.5 (c) and (d). From this point in the study, the focus was directed at orientation distributions in the α matrix and related transformations process as they can be documented by traversing from the unaffected base metal into the affected friction-stir processed zone.

C. FRICTION-STIR PROCESSED NICKEL-ALUMINUM BRONZE

Optical microscopy and OIM were used in analyzing the various regions in the FSP NAB microstructure. The analysis line of traverse is shown in Figure 4.6, starting from the unaffected base metal into the thermomechanically-affected zone (TMAZ) and friction-stir processed nugget just below the tool shoulder (also known as the dynamically recrystallized (DRX) zone).

1. Base Metal

In Figure 4.7(b), the morphology of the α and κ phases was still identifiable in the unaffected region in base metal. Grains in the base metal measured, on the average, approximately 1 mm in diameter, and were readily distinguishable to the naked eye. The OIM grain orientation map in Figure 4.7(d) depicts portions of two such a large grains, which are designated in two different colors. A few small κ particles, which are also randomly colored, are located nearby or within the boundary. Two distinct grain orientations are clearly evident in the (001) pole figure in Figure 4.7 (there are three linearly independent <001> directions for each grain).

2. Thermomechanically-Affected Zone (TMAZ)

Steep gradients in strain, strain rate and temperature are characteristic of FSP and this is evident in steep gradients in microstructure in the TMAZ. Grain distortion and grain elongation are apparent upon crossing into the TMAZ from base metal, as may be readily discerned in the optical micrograph of Figure 4.8(b). Grain shape changes indicative of shear in a direction aligned with the TD in Figure 4.8(b) are apparent in the upper part of the micrograph. The shear-dominated region appears to extend only about 0.2 mm along the RD, i.e., in a direction normal to the interface between base metal and the TMAZ. Further on into the TMAZ the κ particles as well as α grains have been broken up; the lamellar structure associate with κ_{III} is no longer distinct although the dark regions in the TMAZ may include the κ_{III}. The globular κ_{II} particles appear to be somewhat finer in size but are still distinguishable. It is difficult to discern the effects of deformation in the finer κ_{IV} at this magnification. OIM data corresponding to this region are shown in Figure 4.8(c) and 4.8(d). Comparison of Figures 4.7(c) and 4.8(c) reveals that the distribution of orientations has become more random. Figure 4.8(d) illustrates a fine, somewhat elongated grain structure of grain size < 10 μm; the spread in orientations in the pole figure suggests that these are grains and not subgrains formed due only to recovery effects. Thus, the grain size has been drastically reduced, from 1 mm down to < 10 μm over a very short distance of about 1 mm and this suggests that FSP is accompanied by steep gradients in microstructure as well as in strain, strain rate and temperature. In Figure 4.8(b) and 4.8(d) there is a banded distribution of an unknown

phase that is dark in appearance and apparently formed during the breakup of the microstructure. This may be associated with deformation of regions containing the lamellar κ_{III} (as suggested by the optical microscopy in Figure 4.8(b)) but this was not investigated further in the present effort.

3. Grain-Refined Region

Upon traversing from the TMAZ boundary further on into the FSP nugget, a region was encountered that comprised highly refined grains and a very homogeneous microstructure (Figure 4.9). Optical microscopy in Figure 4.9(b) suggests the presence of very fine, equiaxed grains as well as refined and uniformly dispersed second-phase particles. The microtexture in this region is essentially random, as shown in the pole figure data of Figure 4.9(c). The corresponding OIM grain maps in Figure 4.9(d) show equiaxed and ultra-fine grains having an average grain diameter of 3 μm. The various κ phases are not apparent at the resolution of the grain map in Figure 4.9(d) suggesting that the particles have been broken up during the severe shear plastic deformation encountered in FSP. In the event that such particles are 2 μm or less in size they will be difficult to distinguish by OIM alone, as discussed earlier in this Chapter, and thus complementary techniques involving transmission electron microscopy will be required to provide a complete characterization of these regions. According to the theory of particle-stimulated nucleation (PSN) of recrystallization second-phase particles ~ 1 μm in size may serve as nucleation sites for the formation of new grains [Ref. 33-34]. The very large strains associated with FSP likely have resulted in the formation of fine particles that subsequently serve as nucleation sites for recrystallization. Random textures, such as seen in the pole figure of Figure 4.9(c), are characteristic of PSN [Ref. 33-34].

4. FSP Zone Nugget/Dynamically Recrystallized (DRX) Zone

Figure 4.10 summarizes the microstructure in the FSP nugget just beneath the tool shoulder. Figure 4.10(b) is an optical micrograph showing elongated grains aligned with the shear direction and with a relatively coarser microstructure than further away from the tool shoulder. Large dark regions are again evident. While the texture is still essentially random, as shown in Figure 4.10(c), annealing twins are apparent in the OIM grain map in Figure 4.10(d). The presence of annealing twins indicates that temperatures

in this region attained values sufficient for grain growth during annealing after cessation of deformation. The pole figure in Figure 4.10(c) reflected a random texture which is consistent again with PSN of recrystallization but followed by annealing and grain growth.

The microstructures observed in this region exhibited a wavy band-like pattern within the FSP nugget. This suggests a tendency of the material to have a vertical (along RD) component to the flow as well as flow in a horizontal plane due to shear associated with tool rotation. This behavior has been associated with the stirring action as well as with the design of the FSP tool. During processing, the material is churned and carried from the advancing to the retreating side of the processed zone. Eddy-like features created within the processed region by the tool action, especially directly between the tool shoulder and tip, cause the processed material to be stirred both vertically and horizontally [Ref. 35].

As previously mentioned and observed in Figures 4.7 through 4.10, grain sizes varied greatly from base metal into the TMAZ. Figure 4.11 illustrates this variation in grains size by plotting the grain size versus approximate distance from a reference point located just inside unaffected base metal. Grain size is plotted logarithmically; the grain size is reduced by more than two orders of magnitude within a distance of 2 – 3 mm. The apparent increase in grain size within the FSP nugget reflects higher peak temperatures due to closer proximity to the tool. Histograms representing the distributions of grain-to-grain misorientation angles are included for base metal in Figure 4.11(b) and for the three locations in the TMAZ as Figures 4.11 (c), (d) and (e). These latter locations correspond to the microstructures shown in Figures 4.8 – Figure 4.10. Few grains are represented in base metal due to the coarse grain size. All of the distributions in the TMAZ exhibit low-angle boundaries (up to 10° in misorientation) that are the result of subgrain formation following deformation. High-angle peaks (55° - 60°) reflect twin formation during post deformation annealing. At intermediate misorientation angles (10° - 55°) the experimental distributions are similar to the Mackenzie distribution for the misorientations of randomly oriented cubes [Ref. 36]

D. SHEAR TEXTURES AT THE TMAZ / BASE METAL BOUNDARY

The results of a more detailed study of locations at the TMAZ boundary in the FSP NAB are shown in Figure 4.12. The locations were selected to examine regions on the advancing and retreating sides of the tool as well as locations more or less under the tool. In each location the area selected corresponded to the region of grain distortion such as seen in Figure 4.8(b). In the present analysis the data are presented in the form of {001}, {022} and {111} pole figures for each location. A representation of the spatial orientation of a cubic crystal lattice has been included with each set of pole figures to aid in interpretation of the local orientation.

In all locations a single lattice orientation is evident; the orientation has a <110> near the normal direction of the {022} pole figure indicating that such a direction tends to align with the direction of tool advance. All of the orientations observed in Figure 4.12 are similar to the C type shear texture as described by Canova et al. [Ref. 37]. Pole figures representing this texture component are shown in the form of (111) and (100) pole figures in Figure 4.13 (from Canova, et al. [Ref. 37]). The pole figures in Figure 4.13 are drawn such that the shear direction is downward and the shear plane normal is to the right, i.e., the trace of the shear plane would be a vertical line in each pole figure. Comparison of the data in Figure 4.12 and 4.13 reveals a C-type shear texture at each location examined. In general, the apparent shear plane does not align with the base metal / TMAZ interface although a tendency of the shear plane to rotate about the ND, aligning with the base metal / TMAZ interface in only Figure 4.12(e).

From theoretical assessments of the shear at the base metal / TMAZ boundary it is expected that the active slip systems will tend to align the slip plane with the tangent to the trailing edge of the tool shoulder [Ref. 28]. However, the results of this study suggest an alternate interpretation. As depicted by the red dashed lines in Figures 4.12 (a) through (d), the {111}<110> slip system tends to align with the direction normal to the TMAZ boundary, while it is apparently parallel to the TMAZ boundary only in Figure 4.12 (e). This behavior may be consistent with observations of the material flow during FSP [Ref. 35]. One may recall that during the process, while the material in the FSP region is being stirred (mostly in a horizontal direction), the outlying material just beyond

the TMAZ boundary experiences either an upward or downward component to the flow, as it begins to deform and become entrained in the TMAZ. This vertical flow of material is likely to be perpendicular to the TMAZ boundary, and thus leads to slip systems acting to provide shear normal to the boundary. This is evident in four locations in Figure 4.12: (a), (b), (c), and (d). On the other hand, in the bottom region toward the advancing side, Figure 4.12(e), the material may have deformed with the rotation of the tool (i.e. into the plane of the paper) while in the process of being stirred, and thus resulted in a slip system parallel to the TMAZ boundary. Thus, the {111}<110> slip systems may account for local deformation normal to as well as parallel to the TMAZ boundary and the current results are evidence of both vertical and horizontal components of the shear mechanism dominant in the boundary.

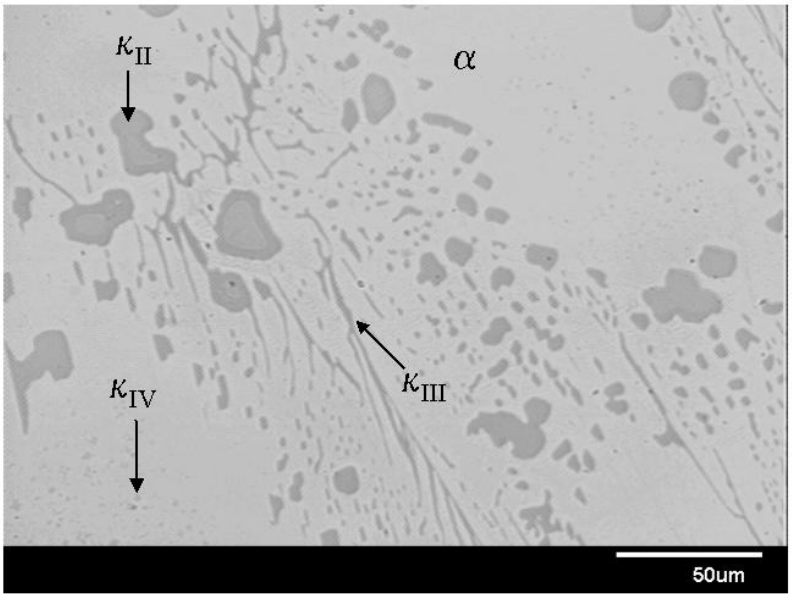

Figure 4.1: As-cast NAB microstructure. Phases observed: light-colored α matrix, globular dendritic κ_{II}, lamellar κ_{III}, and fine κ_{IV} particles within the α matrix. Due to the low iron and nickel contents, κ_I was not observed. Magnification x750.

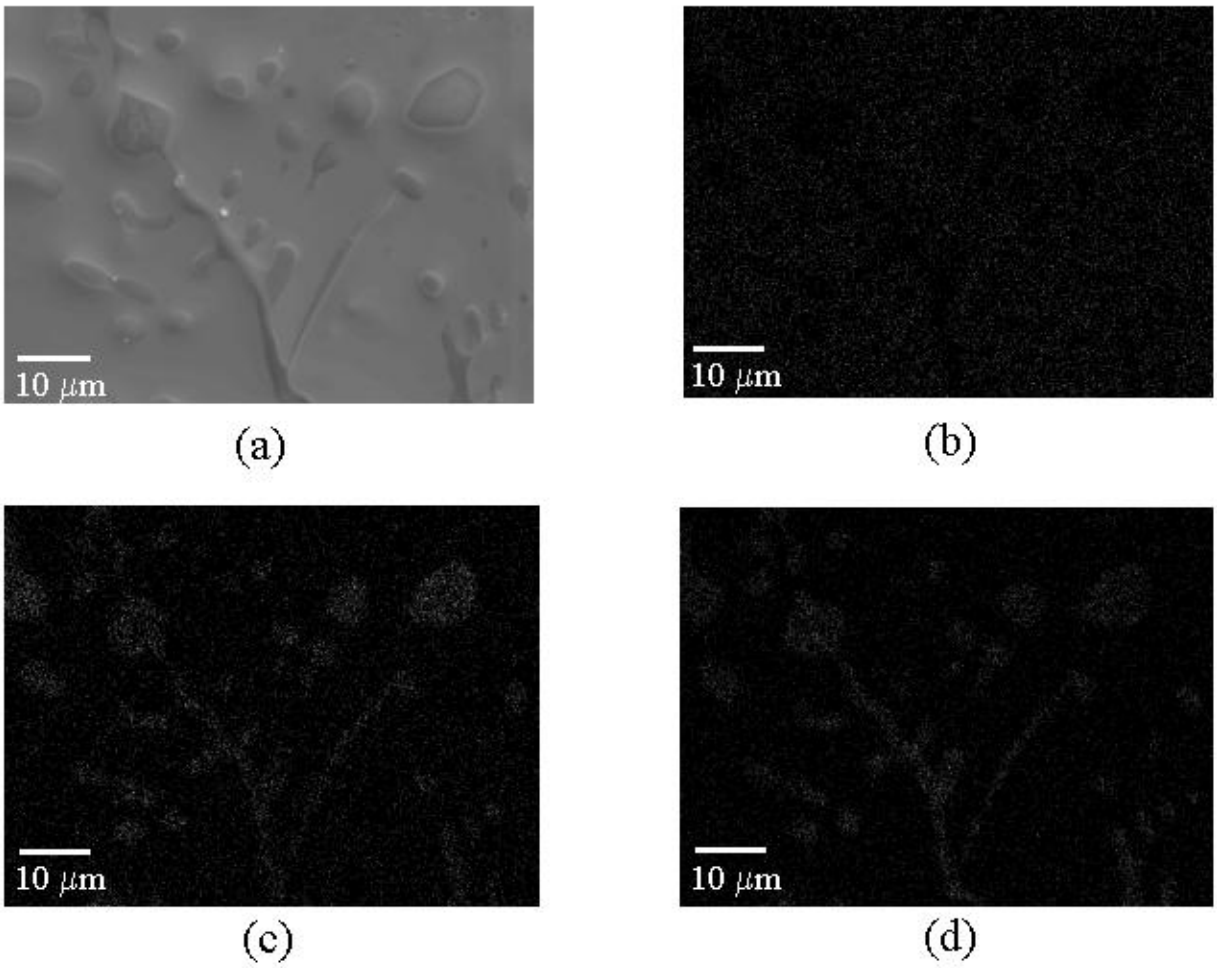

Figure 4.2: Energy-dispersive x-ray (EDX) analysis of as-cast NAB. (a) Secondary electron emission image of NAB microstructure, containing α and κ phases. (b) Copper-rich image. (c) Iron-rich image. (d) Nickel-rich image.

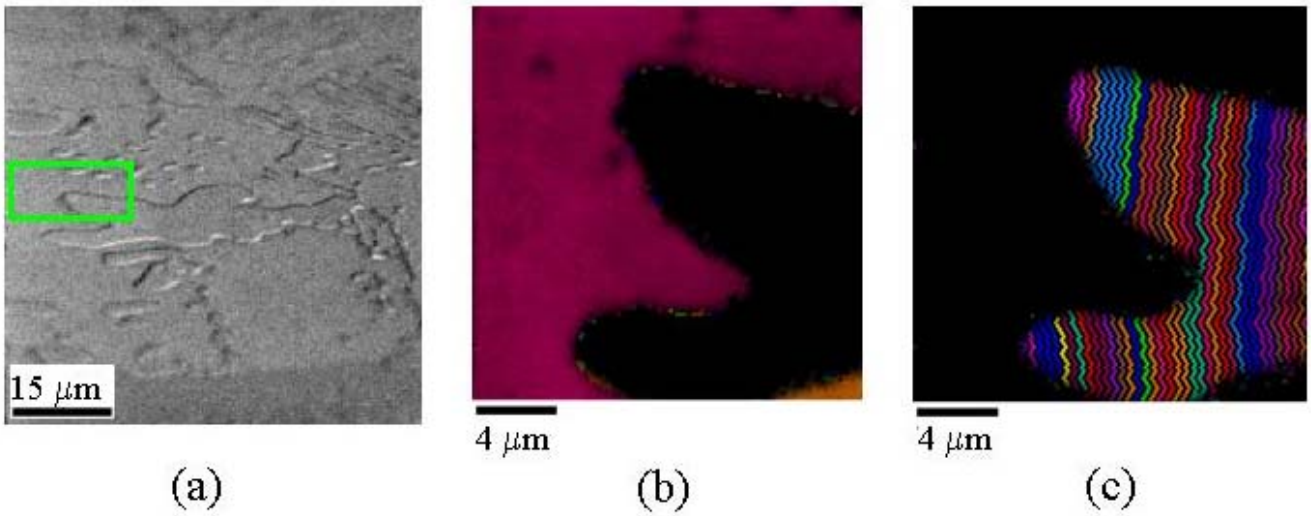

Figure 4.3: OIM phase identification in as-cast NAB. (a) Scanning electron microscope image of NAB sample tilted at 70 degrees, with scanned area outlined by green box. (b) Grain orientation map, identified by OIM as the copper-rich fcc α phase (matrix). (c) OIM default systematic interpretation of nearly identical crystal structures of κ phases. OIM is unable to distinguish between $\kappa_{II,IV}$ and κ_{III} phases due to very similar crystal structures.

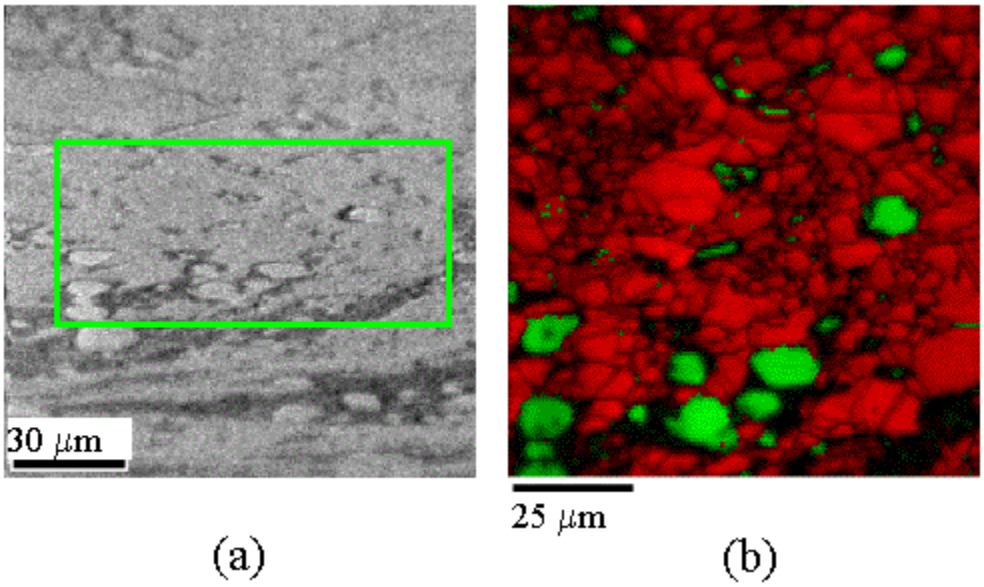

Figure 4.4: OIM phase identification using α phase and single κ phase. (a) SEM image, (b) OIM grain orientation map, with α phase in red and single κ phase in green.

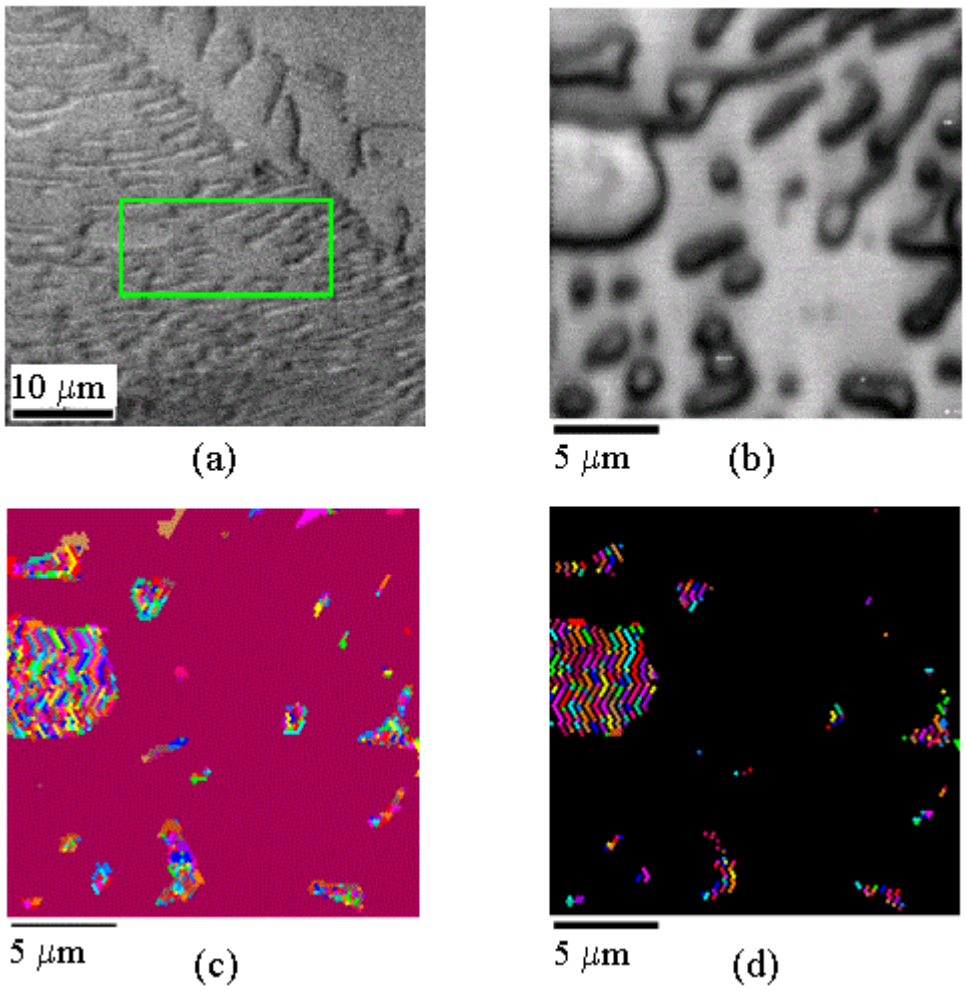

Figure 4.5: Limit of resolution and phase identification. (a) Scanning electron microscope image of NAB sample tilted at 70 degrees, with scanned area outlined by green box. (b) Image quality grayscale clearly shows second phase particle morphology. (c) Grain orientation map including all phases. The copper-rich fcc α phase (matrix) is easily identified by OIM and arbitrarily designated with a maroon color. The α phase is clearly distinguishable from the κ particles. (d) OIM default systematic interpretation of nearly identical crystal structures of κ phases is apparent in the rainbow pattern. OIM is unable to distinguish between $\kappa_{II,IV}$ and κ_{III} phases due to very similar crystal structures. Smaller κ particles (less than 2 μm) in (b) are not observed in the grain maps (c) and (d), and are identified as part of α matrix.

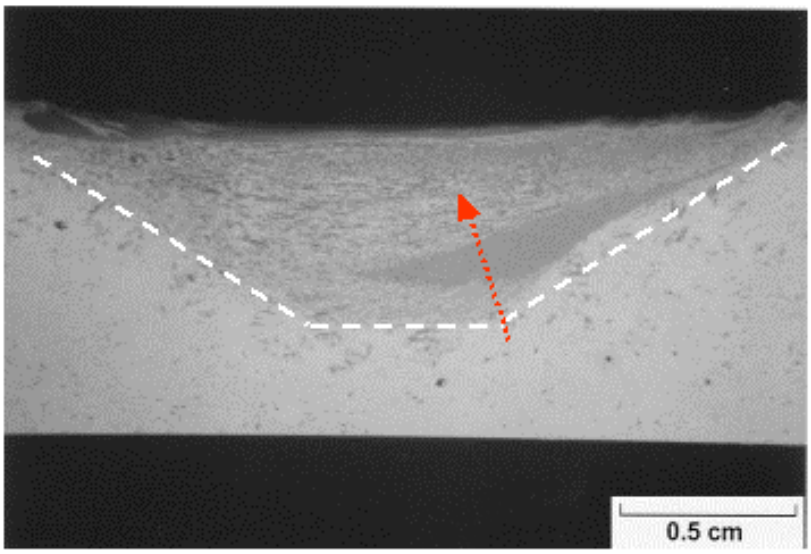

Figure 4.6: Optical micrograph of friction-stir processed NAB *(Courtesy of M.W. Mahoney, RSC)*. The white dashed line marks the thermomechanically-affected zone (TMAZ) boundary. The red dotted line is the analysis line of traverse from the unaffected base metal into the FSP region.

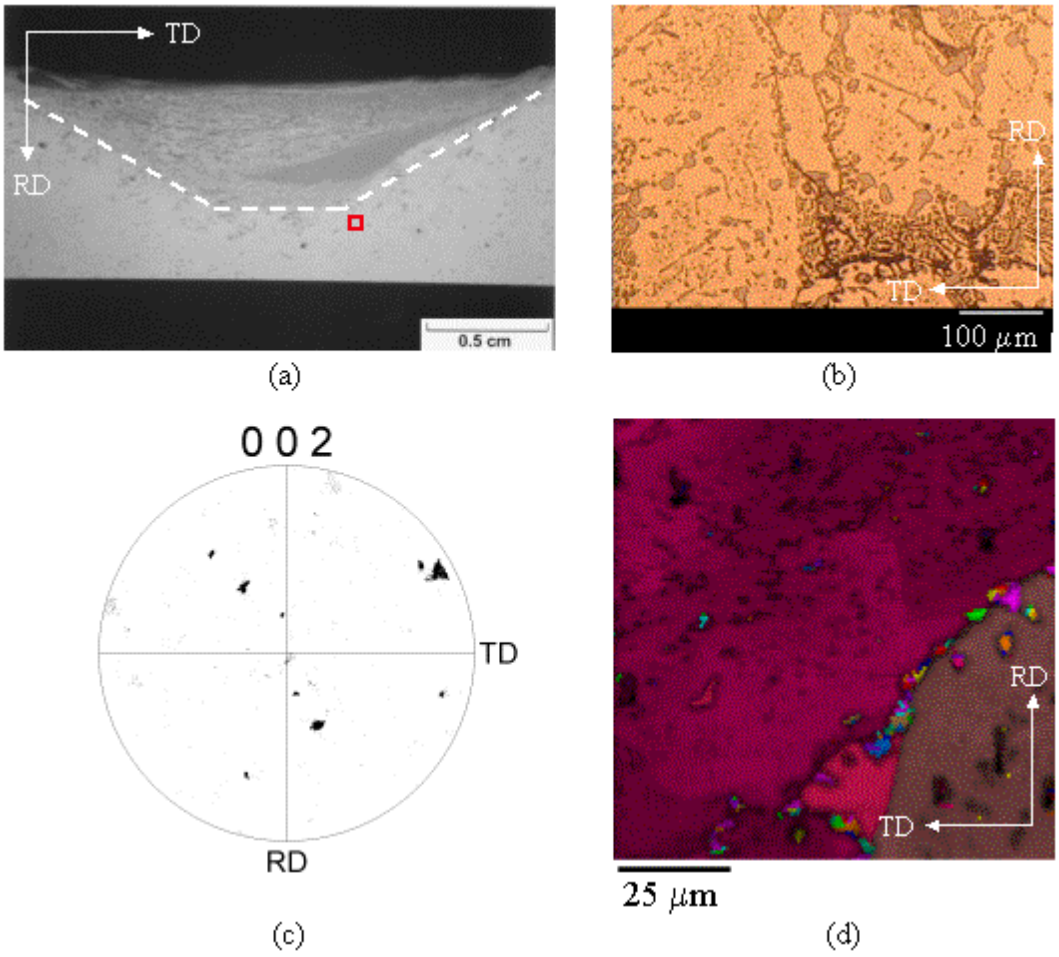

Figure 4.7: Base metal microstructure and grain orientation of friction-stir processed NAB. (a) Optical micrograph of FSB NAB, with scanned area outlined in red. *(Micrograph courtesy of M.W. Mahoney, RSC.)* (b) Optical micrograph depicting phase morphology in NAB base metal (x370 magnification). (c) Base metal {001} pole figure from OIM, indicating well-defined grain orientations. (d) OIM grain orientation map of area containing two large grains (~ 1 mm in diameter).

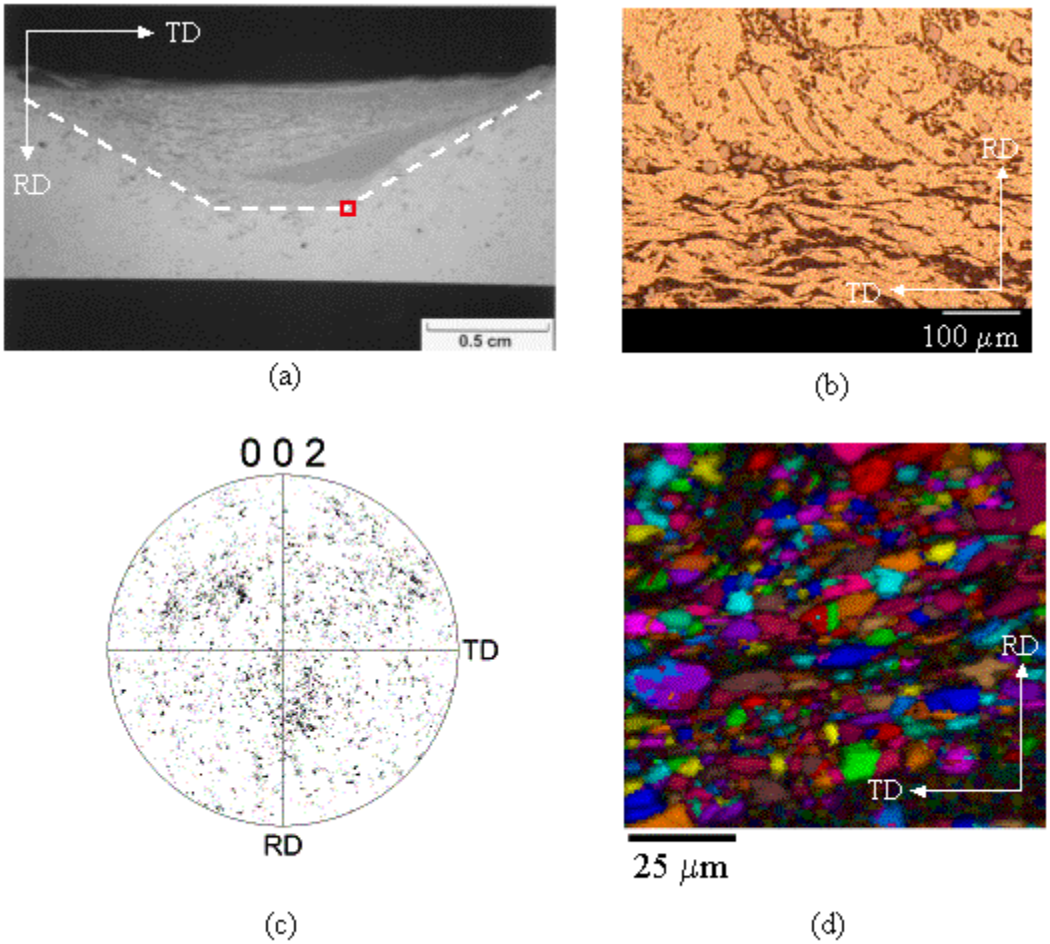

Figure 4.8: Thermomechanically-affected zone (TMAZ) boundary microstructure and grain orientation of friction-stir processed NAB. (a) Optical micrograph of FSp NAB, with scanned area outlined in red. *(Micrograph courtesy of M.W. Mahoney, RSC.)* (b) Optical micrograph depicting phase morphology along NAB TMAZ boundary (x370 magnification). (c) {001} pole figure from OIM, indicating beginnings of random textured grain orientations as grains become distorted. (d) OIM grain orientation map of area showing grain distortion and elongation, as well as drastic reduction of grain size (~ 5-10 μm).

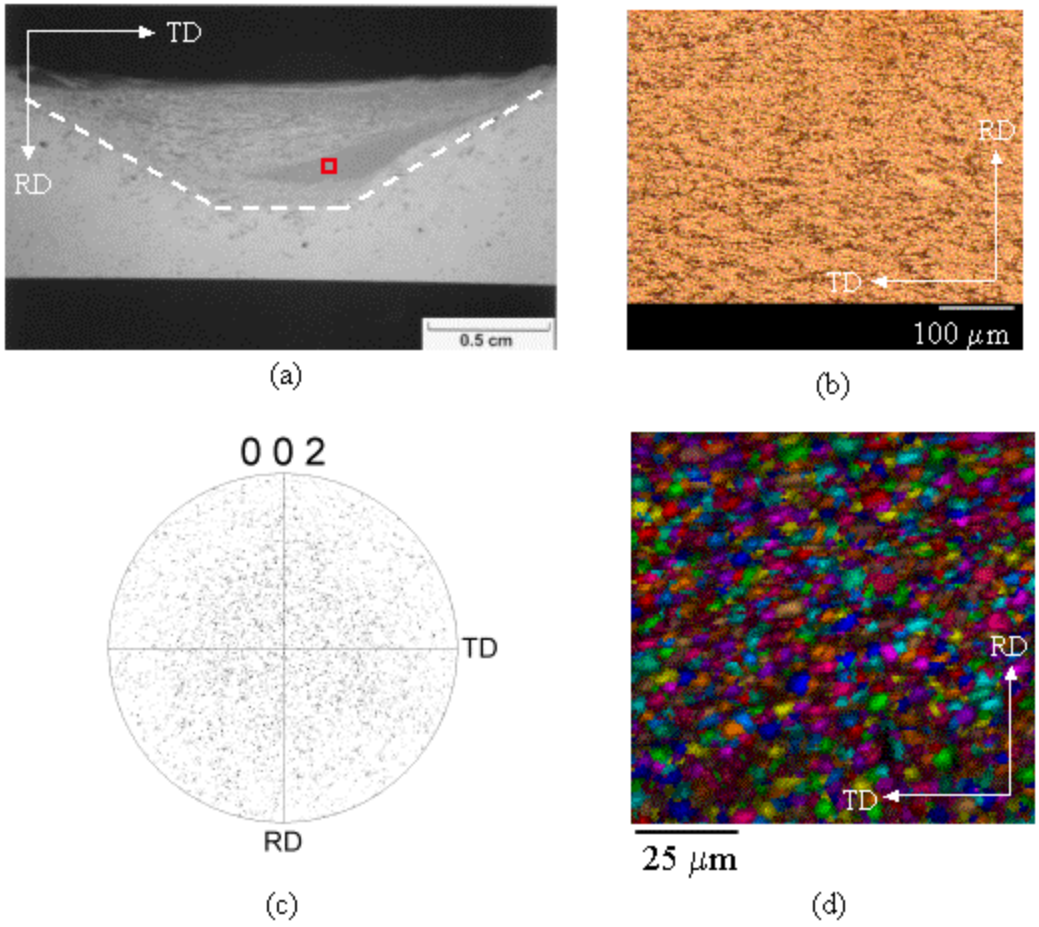

Figure 4.9: Grain-refined region microstructure and grain orientation of friction-stir processed NAB. (a) Optical micrograph of FSP NAB, with scanned area outlined in red. *(Micrograph courtesy of M.W. Mahoney, RSC.)* (b) Optical micrograph depicting homogeneous microstructure within NAB grain-refined band in TMAZ (x370 magnification). (c) {001} pole figure from OIM, indicating uniform randomly textured grain orientations as well as recrystallized grains. (d) OIM grain orientation map of area showing ultra-fine recrystallized grains having an average grain size diameter ~ 3 - 4 μm.

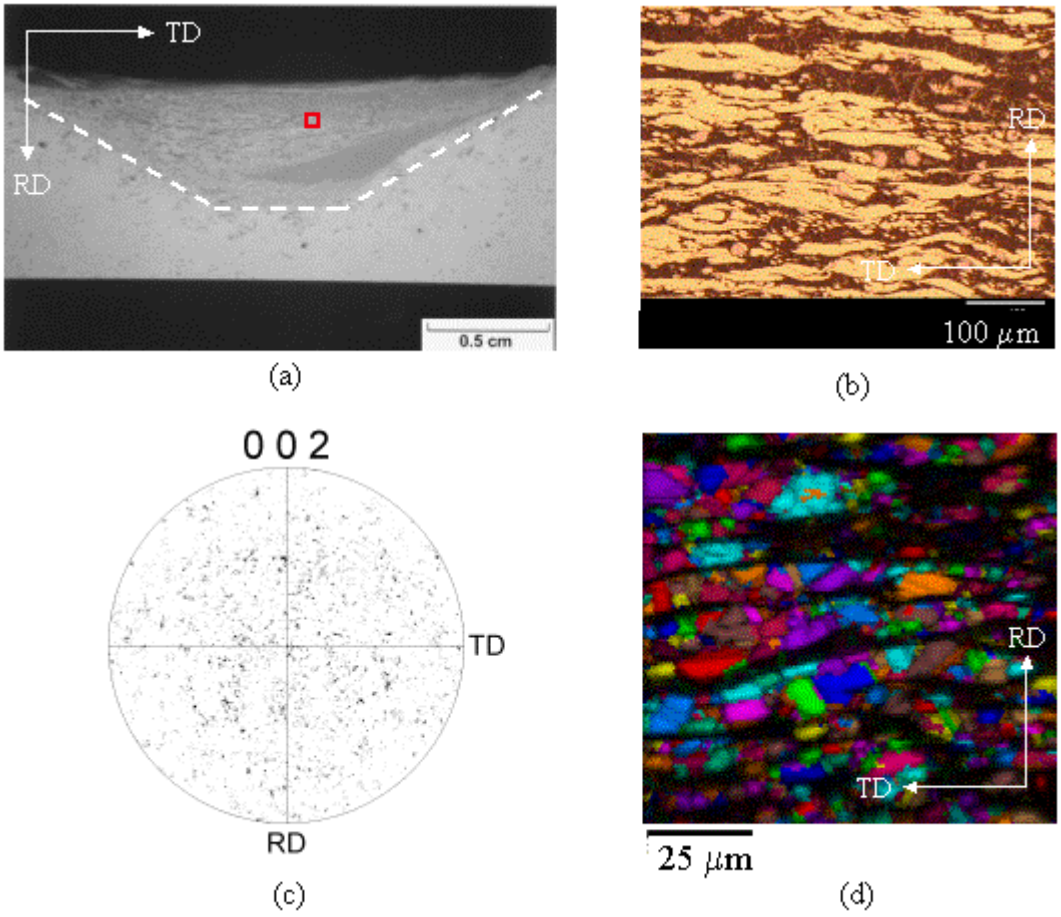

Figure 4.10: FSP NAB microstructure and grain orientation in TMAZ region just beneath the tool shoulder. (a) Optical micrograph of FSP NAB, with scanned area outlined in red. *(Micrograph courtesy of M.W. Mahoney, RSC.)* (b) Optical micrograph depicting coarser elongated grains (x370 magnification). (c) {001} pole figure from OIM, indicating randomly textured grain orientations. (d) OIM grain orientation map of area showing elongated grains in a wavy band-like pattern. Also apparent are annealing twins within grains, indicative of post-deformation annealing.

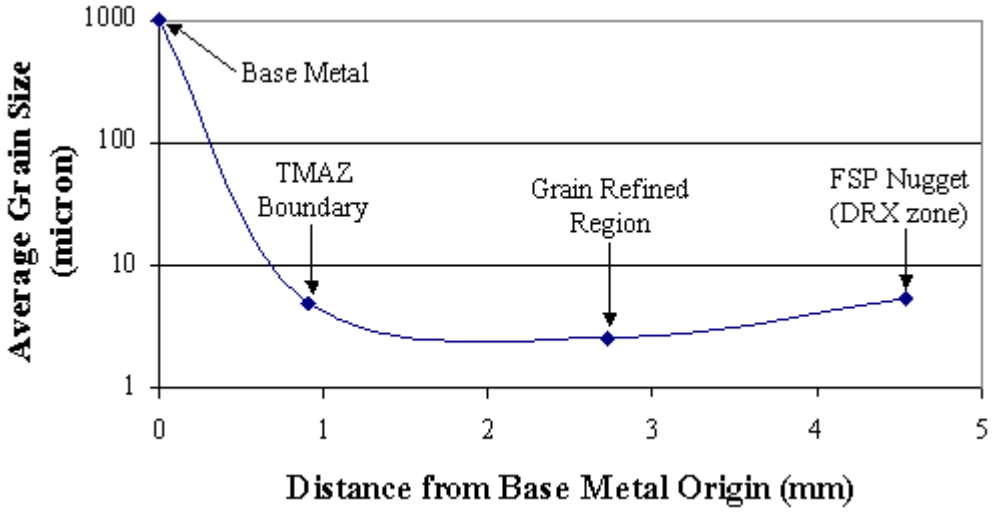

(a)

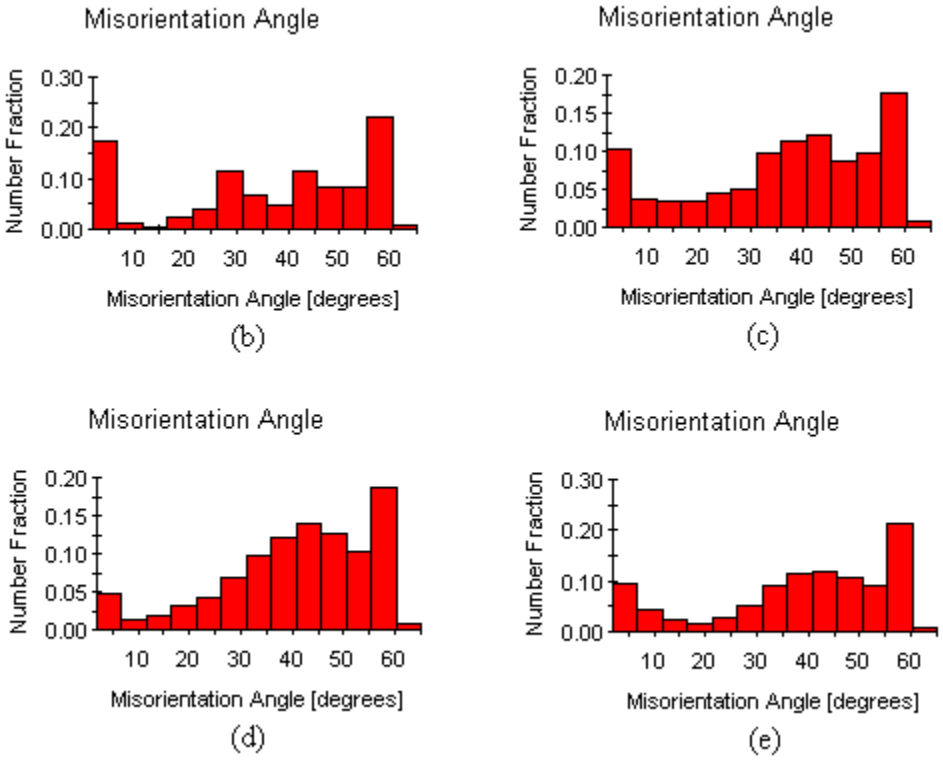

Figure 4.11: (a) Grain size distribution during the traverse analysis from NAB base metal into FSP nugget. Grain size drastically reduces across a very short distance along the TMAZ boundary. Ultra-fine grains emerge in the grain-refined region. Grains are observed to coarsen slightly within the FSP nugget, where post-deformation annealing may have occurred. Corresponding grain misorientation angle histograms in (b) base metal, (c) TMAZ boundary, (d) grain-refined region, and (e) FSP nugget/DRX zone.

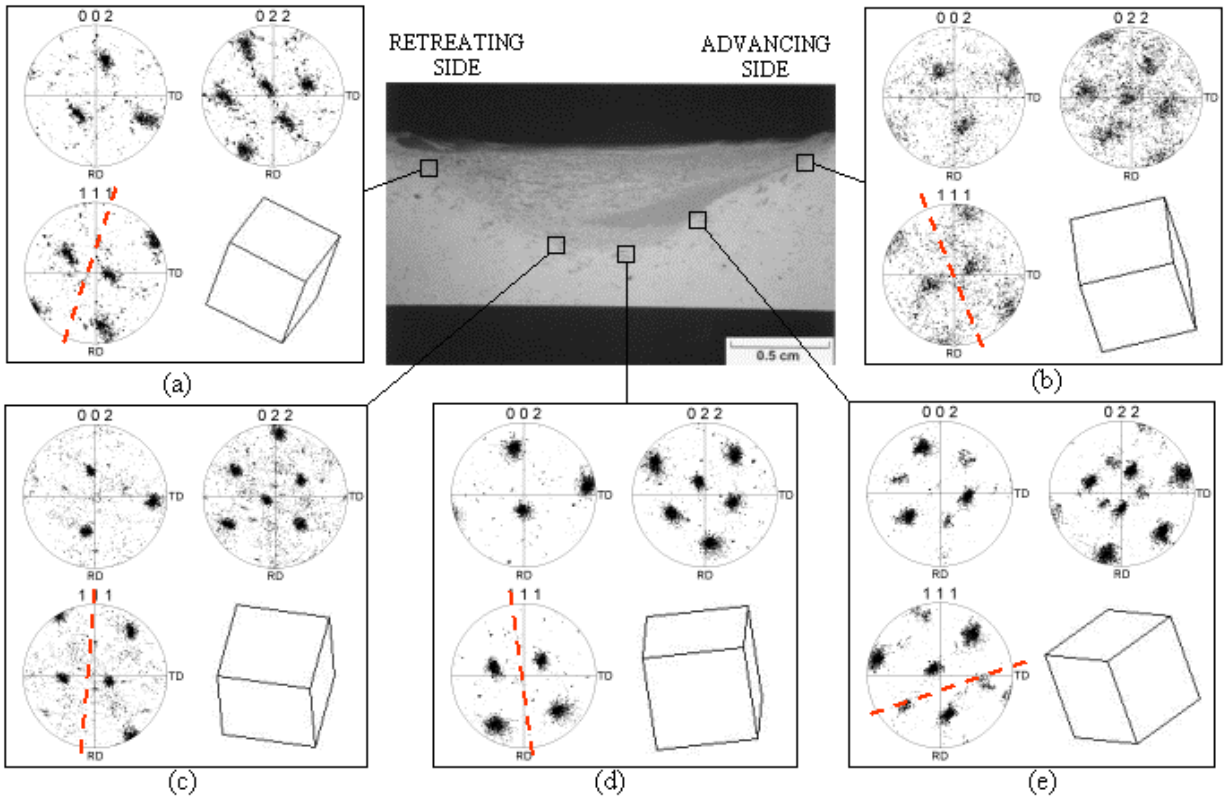

Figure 4.12: Montage of OIM pole figures of regions along the TMAZ boundary in a friction-stir processed NAB: (a) retreating side top, (b) advancing side top, (c) retreating side bottom, (d) bottom center, and (e) advancing side bottom. Lattice cubes are included with each set of pole figures to give a quick interpretation of the grain orientations at each location. Red dashed lines indicate the shear direction. *(Micrograph courtesy of M.W. Mahoney, RSC)*

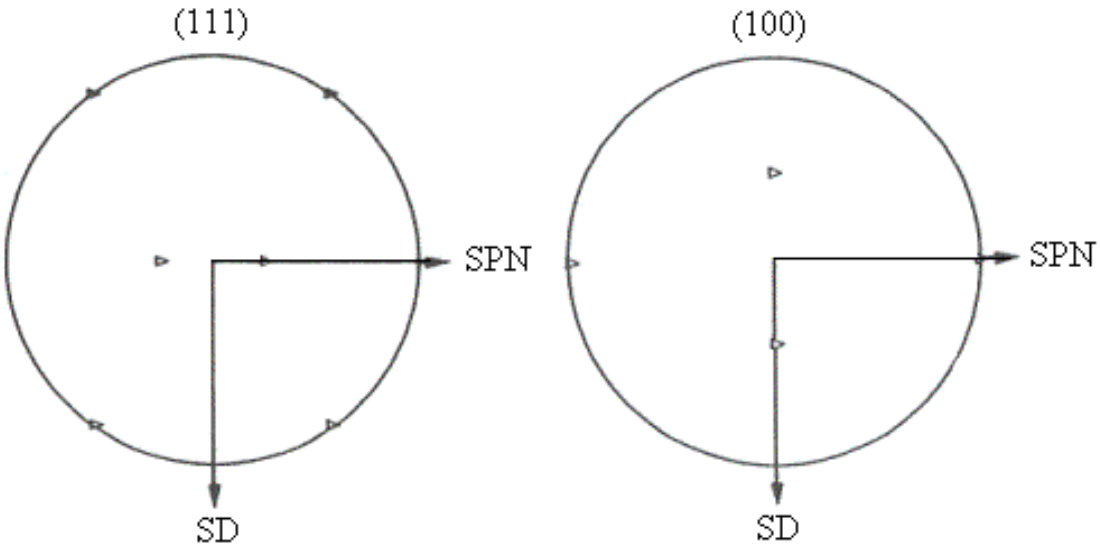

Figure 4.13: (111) and (100) pole figures of the shear "C" texture. SPN represents the shear plane normal direction. SD represents the shear direction. (Modified from Canova, 1984.)

THIS PAGE INTENTIONALLY LEFT BLANK

V. SUMMARY AND CONCLUSIONS

A. SUMMARY AND CONCLUSIONS

The following general conclusions can be drawn from the application of OIM to the study of friction-stir processed nickel-aluminum bronze.

(1) The OIM program is capable of distinguishing between α and κ phase crystal structures in NAB. However, due to the similar interatomic distances of the κ phase $D0_3$ and B2 crystal structures, OIM is unable to differentiate between their associated EBSPs.

(2) Energy-dispersive x-ray (EDX) analysis may be used in conjunction with OIM program to improve identification among the κ phases.

(3) Traversing from the unaffected base metal into the friction-stir processed NAB nugget, analysis of the microstructures revealed grain distortion and elongation at the base metal / TMAZ boundary, which was indicative of material deformation during stirring. Recrystallization became evident within the FSP region in the form of ultra-fine grains in a homogeneous, randomly-textured microstructure. Annealing twins apparent in the FSP elongated grains signified annealing after the occurrence of plastic deformation.

(4) The wavy band-like pattern observed in the FSP region denoted the horizontal material flow, which resulted from the rotation of the tool during processing.

(5) The presence of C-type shear textures but with {111}<110> slip systems normal to the base metal / TMAZ boundary in many locations indicated the vertical component of material flow during processing, while the same slip systems parallel to the boundary suggested material flow in the direction of tool advance.

B. RECOMMENDATIONS FOR FUTHER STUDY

It is recommended that further study in the area of transmission electron microscopy (TEM) and NAB deformation testing be carried out. Specifically, investigations should include more accurate phase identification within both base metal and the TMAZ. Further study is recommended on the effect of deformation on NAB phases and microstructures annealed at discrete temperatures, in order to separately simulate the intense strain, strain rate and temperature effects present during the FSP process. Continued phase and microstructure analysis may be conducted on FSP NAB samples having varied parameters, such as varied tool rotational and travel speed, different tool shapes, multiple passes. Research in this area may aid in the production of an optimum FSP microstructure and eventually lead to superior material properties.

LIST OF REFERENCES

1. Duma, J.A., "Heat Treatments For Optimizing Mechanical and Corrosion Resisting Properties of Nickel-Aluminum Bronzes," *Naval Engineers Journal*, v. 87, p. 45-64, 1975.

2. Metals Handbook, 9th Ed., v. 2, Properties & Selections: Nonferrous Alloys and Pure Metals.

3. Military Specifications For Bronze, Nickel-Aluminum (UNS C95800), Castings For Seawater Service (MIL-B-24480A), 20 June 1985.

4. American Society for Testing and Materials (ASTM) B148 – 93a, Standard Specification for Aluminum-Bronze Sand Castings.

5. Sahoo, M., "Structure and Mechanical Properties of Slow-Cooled Nickel-Aluminum Bronze Alloy C95800," *AFS Trans*, v. 90, p. 913-926, 1982.

6. Wenschot, P., "The Properties of Ni-Al Bronze Sand Cast Ship Propellers in Relation to Section Thickness," *International Shipbuilding Progress*, v. 34, p. 112-123, 1987.

7. Ferrara, R.J. and Caton, T.E., "Review of Dealloying of Cast Aluminum Bronze and Nickel-Aluminum Bronze Alloys in Sea Water Service," *Materials Performance*, v. 21, No. 2, p. 30-34, 1982.

8. G.W. Lorimer, F. Hasan, J. Iqbal, N. Ridley, "Observation of Microstructure and Corrosion Behaviour of Some Aluminum Bronzes," *British Corrosion Journal,* v. 21, p. 244-248, 1986.

9. Culpan, E.A. and Rose, G., "Corrosion Behaviour of Cast Nickel Aluminium Bronze in Sea Water," *British Corrosion Journal,* v. 14, p. 160-166, 1979.

10. W.M. Thomas, E.D. Nicholas, J.C. Needham, M.G. Murch, P. Templesmith and C.J. Dawes, "Friction Stir Butt Welding," G.B. Patent Application No. 9125978.8, Dec. 1991; U.S. Patent No. 5460317, Oct. 1995.

11. Mishra, R.S. and Mahoney, M.W., "Friction Stir Processing: A New Grain Refinement Technique to Achieve High Strain Rate Superplasticity in Commercial Alloys," *Materials Science Forum,* v. 357-359, p. 507-514, 2001.

12. P.B. Berbon, W.H. Bingel, R.S. Mishra, C.C. Bampton and M.W. Mahoney, "Friction Stir Processing: A Tool to Homogenize Nanocomposite Aluminum Alloys," *Scripta Materialia*, v. 44, p. 61-66, 2001.

13. R.S. Mishra, M.W. Mahoney, S.X. McFadden, N.A. Mara and A.K. Mukherjee, "High Strain Rate Superplasticity In A Friction Stir Processed 7075 Al Alloy," *Scripta Materialia*, v. 42, p. 163-168, 2000.

14. Culpan, E.A. and Rose, G., "Microstructural Characterization Of Cast Nickel Aluminium Bronze," *Journal of Materials Science*, v. 13, p. 1647-1657, 1978.

15. Weston, G.M., "Survey of Nickel-Aluminium-Bronze Casting Alloys on Marine Applications," Australia Dept. of Defence Report, DSTO MRL, Melbourne, Victoria, MRL-R-807, 1981.

16. Brezina, P, "Heat Treatment of Complex Aluminum Bronzes," *Int. Met. Rev*., v. 27, n. 2, p. 77-120, 1982.

17. D.M. Lloyd, G.W. Lorimer and N. Ridley, "Characterization of Phases in a Nickel-Aluminium Bronze," *Metals Technology*, v. 7, p. 114-119, 1980.

18. F. Hasan, G.W. Lorimer and N. Ridley, "Precipitation During the Tempering of a Nickel-Aluminium Bronze," *Proc. Intl. Conf. On Solid to Solid Phase Transformations*, Pittsburgh, PA, p. 745-749, 1982.

19. F. Hasan, A. Jahanafrooz, G.W. Lorimer and N. Ridley, "The Morphology, Crystallography, and Chemistry of Phases in As-Cast Nickel-Aluminum Bronze," *Met. Trans A*, v. 13a, p.1337-1345, 1982.

20. F. Hasan, G.W. Lorimer and N. Ridley, "Crystallography of Martensite in a Cu-10Al-5Ni-5Fe Alloy," *Journal de Physique*, v. 43, p. C4 653-C4 658, 1982.

21. A. Jahanafrooz, F. Hasan, G.W. Lorimer and N. Ridley, "Microstructural Development in Complex Nickel-Aluminum Bronze," *Met. Trans A*, v. 14a, p. 1951-1956, 1983.

22. F. Hasan, G.W. Lorimer and N. Ridley, "Tempering of Cast Nickel-Aluminium Bronze," *Metal Science*, v. 17, p. 289-295, 1983.

23. F. Hasan, J. Iqbal and N. Ridley, "Microstructure of As-Cast Aluminium Bronze Containing Iron," *Mat. Sci and Tech*, v. 1, p. 312-315, 1985.

24. Weill-Couly, P. and Arnaud D., "Influence De La Composition Et De La Structure Des Cupro-Aluminiums Sur Leur Comportment En Service," *Fonderie*, no. 322, p. 123-135, 1973.

25. D.E. Bell, MS Thesis, "Microstructural Development and Corrosion Resistance of Laser-Welded Nickel-Aluminum Bronze," Pennsylvania State University, PA, 1994.

26. K.V. Jata and S.L. Semiatin, “Continuous Dynamic Recrystallization During Friction Stir Welding of High Strength Aluminum Alloys,” *Scripta Materialia*, v. 43, p. 743-749, 2000.

27. G. Liu, L.E. Murr, C.S. Niou, J.C. McClure and F.R. Vega, ”Microstructural Aspects of the Friction Stir Welding of 6061-T6 Aluminum,” *Scripta Materialia*, v. 37, p. 355-361, 1997.

28. D.P. Field, T.W. Nelson, Y. Hovanski and K.V. Jata, “Heterogeneity of Crystallographic Texture in Friction Stir Welds of Aluminum,” *Met. And Mat. Trans. A*, v. 32a, p. 2869-2877, 2001.

29. Orientation Imaging Microscopy (OIM) Data Collection User Manual, ver. 1.0, TexSEM Laboratories, Inc., 1998.

30. Orientation Imaging Microscopy (OIM) Analysis, ver. 3.0, TexSEM Laboratories, Inc., 2000.

31. D.L. Swisher, MS Thesis, “Production of Ultra-Fine Grains and Evolution of Grain Boundaries During Severe Plastic Deformation of Aluminum and its Alloys,” Naval Postgraduate School, Monterey, CA, 2000.

32. S.D. Terhune, Z. Horita, M. Nemoto, Y. Li, T.G. Langdon and T.R. McNelley, ”The Evolution of Microtexture and Grain Boundary Character during ECA Pressing of Pure Aluminum,” *Intl. Conf. On Recrystallization and Related Phenomena*, p. 515-522, 1999.

33. Doherty, R.D., Hughes, D.A., Humpreys, F.J., Jonas, J.J., Juul Jensen, D., Kassner, M.E., King, W.E., McNelley, T.R., McQueen, H.J., and Rollett, A.D., *Mater. Sci. Eng. A*, v. A238, p. 219, 1997.

34. Humphreys, F.J., *Acta Metall.*, v. 25, p. 1323, 1977.

35. Private communications, M.W. Mahoney, Rockwell Science Center, Thousand Oaks, CA, September 2002.

36. Mackenzie, J.K., *Biometrica*, v. 45, p. 229, 1958.

37. G.R. Canova, U.F. Kocks and J.J. Jonas, “Theory of Torsion Texture Development,” *Acta Metall.*, v. 32, p. 211-226, 1984.

38. Randle, V. and Engler, O., Introduction to Texture Analysis: Macrotexture, Microtexture and Orientation Mapping, Gordon and Breach Science Publishers, The Netherlands, 2000.

THIS PAGE INTENTIONALLY LEFT BLANK

INITIAL DISTRIBUTION LIST

1. Defense Technical Information Center
   Ft. Belvoir, Virginia

2. Dudley Knox Library
   Naval Postgraduate School
   Monterey, California

3. Engineering and Technology Curricular Office, Code 34
   Naval Postgraduate School
   Monterey, California

4. Department Chairman, Code ME/Kw
   Naval Postgraduate School
   Monterey, California

5. Professor Terry R. McNelley, Code ME/Mc
   Naval Postgraduate School
   Monterey, California

6. LT Assunta M. Cuevas
   Oxnard, California

7. Dr. Leo Christodoulou
   DARPA/DSO
   Arlington, Virginia

8. Murray W. Mahoney
   Rockwell Science Center
   Thousand Oaks, California

9. William Palko
   Naval Surface Warfare Center
   Carderock Division
   West Bethesda, Maryland